Published in final edited form as:

Cell Rep. 2021 April 13; 35(2): 108966. doi:10.1016/j.celrep.2021.108966.

UTX promotes CD8+ T cell-mediated antiviral defenses but reduces T cell durability

Joseph E. Mitchell[1,2], **Makayla M. Lund**[1], **Josh Starmer**[1], **Kai Ge**[3], **Terry Magnuson**[1,4], **Karl B. Shpargel**[1,*], **Jason K. Whitmire**[1,2,4,5,*]

[1]Department of Genetics, UNC-Chapel Hill School of Medicine, Chapel Hill, NC 27599, USA

[2]Department of Microbiology & Immunology, UNC-Chapel Hill School of Medicine, Chapel Hill, NC 27599, USA

[3]Adipocyte Biology and Gene Regulation Section, National Institute of Diabetes and Digestive and Kidney Diseases, National Institutes of Health, Bethesda, MD 20892, USA

[4]Lineberger Comprehensive Cancer Center, UNC-Chapel Hill School of Medicine, Chapel Hill, NC 27599, USA

[5]Lead contact

SUMMARY

Persistent virus infections can cause pathogenesis that is debilitating or lethal. During these infections, virus-specific T cells fail to protect due to weakened antiviral activity or failure to persist. These outcomes are governed by histone modifications, although it is unknown which enzymes contribute to T cell loss or impaired function over time. In this study, we show that T cell receptor-stimulated $CD8^+$ T cells increase their expression of UTX (ubiquitously transcribed tetratricopeptide repeat, X chromosome) to enhance gene expression. During chronic lymphocytic choriomeningitis virus (LCMV) infection in mice, UTX binds to enhancers and transcription start sites of effector genes, allowing for improved cytotoxic T lymphocyte (CTL)-mediated protection, independent of its trimethylation of histone 3 lysine 27 (H3K27me3) demethylase activity. UTX also limits the frequency and durability of virus-specific $CD8^+$ T cells, which correspond to increased expression of inhibitory receptors. Thus, UTX guides gene expression patterns in $CD8^+$ T cells, advancing early antiviral defenses while reducing the longevity of $CD8^+$ T cell responses.

Graphical abstract

*Correspondence: karl_shpargel@med.unc.edu (K.B.S.), jwhitmir@email.unc.edu (J.K.W.).

AUTHOR CONTRIBUTIONS

J.E.M., K.B.S., J.S., and J.K.W. designed experiments and analyzed data resulting from experiments. J.E.M. and M.M.L. performed *in vivo* experiments, including mouse breeding, virus injections, plaque assays, and T cell responses. J.S. analyzed RNA-seq data from FACS T cells. K.B.S. performed and analyzed CUT&RUN analyses. K.G. generated the $UTX^{KI/KI}$ mice. J.E.M. and J.K.W wrote the manuscript.

SUPPLEMENTAL INFORMATION

Supplemental information can be found online at https://doi.org/10.1016/j.celrep.2021.108966.

DECLARATION OF INTERESTS

The authors declare no competing interests.

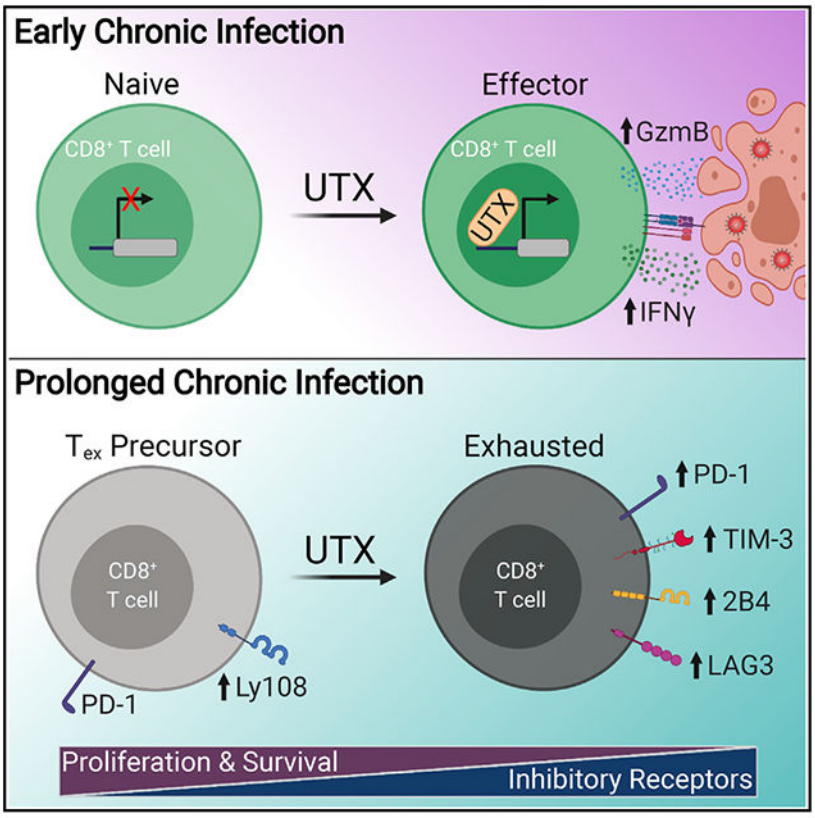

In brief

T cells fail to eliminate chronic virus infections due to alterations in gene expression that undermine their activity. In this study, Mitchell et al. identify a histone-modifying enzyme that promotes effector gene expression and CTL activity early on yet reduces T cell survival, leading to infection persistence.

INTRODUCTION

Disseminating virus infections, such as HIV, hepatitis C virus, and hepatitis B virus, cause significant health burdens for millions of people worldwide (Virgin et al., 2009). While acute infections induce long-lived protective memory T cells, persistent infections in patients or mice result in virus-specific $CD8^+$ T cells that are functionally impaired and unable to provide immune defense (Wherry and Kurachi, 2015). Such “exhausted” T cells arise through altered differentiation events that occur when T cells are exposed to prolonged periods of virus replication and inflammation. During ongoing infections, T cells express increased amounts of membrane-bound inhibitory receptors, including programmed cell death protein-1 (PD-1), lymphocyte activation gene-3 (LAG-3), T cell immunoglobulin and mucin domain-containing-3 (TIM-3), 2B4 (CD244), and others (Blackburn et al., 2009; Kahan et al., 2015; Wherry et al., 2007). These inhibitory receptors cooperatively restrict T cell functions by interfering with proximal T cell receptor (TCR) signaling, costimulatory

receptor signaling, or by altering gene expression to disable antiviral activity (Wherry and Kurachi, 2015).

Checkpoint blockade therapies, which interfere with PD-1 and/or other inhibitory receptors, can transiently restore function to a subset of virus-specific $CD8^+$ T cells, particularly those expressing low-intermediate amounts of PD-1 (Barber et al., 2006; Im et al., 2016; Pauken et al., 2016). However, T cells that are PD-1^{hi} fail to recover when PD-1-PD-ligand (PD-L)1/2 interactions are blocked, as they have terminally differentiated into an exhausted state that is maintained through epigenetic mechanisms, including alterations in DNA methylation, histone 3 lysine 27 (H3K27) methylation, and H3K4 acetylation that regulate gene expression. The epigenetic landscape and transcriptional profile of exhausted $CD8^+$ T cells are distinct from those of naive, effector, and memory subsets (Pauken et al., 2016; Scott-Browne et al., 2016; Sen et al., 2016) and include alterations at the *Pdcd1* locus (Bally et al., 2016; Ghoneim et al., 2017; Lu et al., 2014; Sen et al., 2016; Youngblood et al., 2011; Zhang et al., 2014).

UTX (ubiquitously transcribed tetratricopeptide repeat, X chromosome; *KMD6A* [lysine demethylase 6A]) is a member of the Jumonji-C (JmjC) family of histone demethylases (Agger et al., 2007). *UTX* is located on the X chromosome and escapes X inactivation (Greenfield et al., 1998). Females lacking part or all of an X chromosome develop Turner syndrome, which is characterized by immune deficiencies in immunoglobulin and T cells subsets, including T follicular helper (Tfh) cells, and susceptibility to chronic otitis media (Cacciari et al., 1981; Cook et al., 2015; Jensen et al., 1976; Mock et al., 2000; Thrasher et al., 2016). Whereas EZH2 catalyzes the trimethylation of H3K27 (H3K27me3) to silence genes and can impact T cell commitment to memory or certain lineages (Gray et al., 2017; Yang et al., 2015), UTX and JMJD3 counter EZH2 by removing repressive methyl groups from H3K27 to permit gene transcription. UTX functions at regions proximal to transcription start sites (TSSs), and transitions poised enhancers into an active state to increase gene expression (Beyaz et al., 2017; Wang et al., 2017; Yoo et al., 2016). UTX interacts with transcription factors and epigenetic modifiers, such as KMT2D (MLL4), that can have similar functions in development (Shpargel et al., 2020) and can promote gene expression at specific loci (Froimchuk et al., 2017; Wang et al., 2017; Yoo et al., 2016). For example, UTX can associate with the transcription factors T-bet and eomesodermin to induce chromatin remodeling at the *Ifng* promoter (Miller et al., 2010). Some UTX-dependent gene expression can occur independent of its demethylase activity (Miller et al., 2010; Shpargel et al., 2012; Yoo et al., 2016). UTX is expressed ubiquitously, including in T cells at different stages of development (Cook et al., 2015), and is required for fetal development (Dalgliesh et al., 2010; Jin et al., 2011; Lan et al., 2007; Lee et al., 2012; Shpargel et al., 2012). UTX contributes to gene expression and plays multiple functions in development, health, and disease, although its role in $CD8^+$ T cell responses is unclear.

In this study, we examined the effect of UTX on antiviral $CD8^+$ T cell responses. Upon activation, $CD8^+$ T cells increased expression of UTX and reduced levels of H3K27me3. Mice with a T cell-specific deletion in UTX were able to resolve acute lymphocytic choriomeningitis virus (LCMV) infection but not a variant (LCMV-A22) that widely disseminates and establishes chronic infection. During chronic infection, UTX-deficient

$CD8^+$ T cells expressed lower amounts of antiviral cytokines and granzymes and were less able to protect against infection compared to wild-type (WT) T cells. UTX-deficient $CD8^+$ T cells expressed lower amounts of inhibitory receptors and were resistant to apoptosis, corresponding to a striking outgrowth of cells that were maintained over time during infection. UTX contributed to gene expression in $CD8^+$ T cells and was physically associated with enhancers and TSSs of numerous genes that were expressed in the presence of UTX. T cells expressing a demethylase-dead mutation of UTX resembled WT T cells in frequency and effector molecule expression, suggesting that UTX contributes to T cell effector functions independently of its ability to demethylate H3K27. Collectively, our data show that UTX promotes gene expression patterns that enhance cytotoxic T lymphocyte (CTL) killing but limit $CD8^+$ T cell persistence during chronic infection.

RESULTS

UTX is required for $CD8^+$ T cell-mediated control of disseminated virus infection

We assessed whether UTX expression and subsequent H3K27me3 densities change in $CD8^+$ T cells following TCR activation. At baseline, naive $CD8^+$ T cells expressed moderate amounts of UTX and high amounts of nuclear H3K27me3. UTX concentrations increased and total H3K27me3 levels declined upon *in vitro* TCR stimulation (Figures S1A and S1B), suggesting that UTX may contribute to $CD8^+$ T cell responses. To determine whether UTX impacts antiviral $CD8^+$ T cell responses *in vivo*, we generated $Utx^{fl/fl}LckCre^+$ (UTX-TCD) mice where *Utx* is conditionally deleted in T cells during early stages of T cell development (Cook et al., 2015). UTX-TCD mice resolve acute LCMV-Armstrong infection but fail to control LCMV-A22 infection, a variant that establishes chronic infection for 40–50 days in immune-competent mice (Cook et al., 2015). Because both $CD4^+$ and $CD8^+$ T cells lack UTX in these mice, we sought to disentangle the effects of UTX expression in $CD8^+$ T cells from its contribution to $CD4^+$ Tfh cells (Cook et al., 2015), which promote antiviral antibody titers and virus control. Mice were depleted of $CD4^+$ T cells prior to infection with LCMV-A22 (Figure 1A). Both UTX-TCD and $Utx^{+/+}LckCre^+$ (WT) control mice had similarly high viral loads in the blood at day 7 post-infection. The virus burden declined in the blood and tissues of WT mice by day 21 but remained somewhat higher in UTX-TCD mice (Figures 1B and 1C).

The control and eventual clearance of LCMV depends on antiviral $CD8^+$ T cell responses. Prior to infection, both groups of mice had few activated $CD8^+CD44^+$ T cells, and the frequency and number of these cells were similar (data not shown). Upon LCMV-A22 infection, there was a rapid accumulation of $CD8^+CD44^+$ T cells, which was 2.5-fold higher in the UTX-TCD mice at day 21 post-infection compared to WT mice (Figure 1D). This pool of activated $CD8^+CD44^+$ T cells includes virus-specific T cells of multiple specificities, such as $DbGP_{33–41}$-specific and $DbNP_{396–404}$-specific $CD8^+$ T cells, which were increased 2.7- to 4-fold in the spleens of UTX-TCD mice compared to WT mice (Figures 1E and S2). During the course of chronic LCMV infection, subsets of T cells can persist but progressively lose antiviral activity over time. Early evidence of T cell exhaustion can be seen at day 21 post-infection for both groups of mice, as relatively few GP_{33}-specific $CD8^+$ T cells made interferon (IFN)g (Figure 1F) compared to memory T cells found in acutely

infected mice (85%–90% IFNγ$^+$; Whitmire et al., 2007). The geometric mean fluorescence intensity (gMFI) of IFNγ revealed a trend toward further loss of IFNγ production by T cells in UTX-TCD mice (Figure 1F). In sum, UTX-TCD mice generate more virus-specific CD8$^+$ T cells yet show defects in immune protection and cytokine expression.

UTX intrinsically reduces virus-specific CD8$^+$ T cell numbers during chronic virus infection

Focusing on the effect of UTX on T cell frequencies, we considered that UTX expression in the thymus might affect the precursor frequency of cells that are released to the periphery, potentially altering the frequency of naive CD8$^+$ T cells that are specific for viral epitopes. To ensure that comparisons between donor cell types were accurate, we utilized an adoptive transfer model where a defined number of virus-specific WT and UTX-deficient CD8$^+$ T cells could be compared in the same recipient mice (Figure 2A). UTX-TCD mice were crossed with LCMV-specific TCR-transgenic P14 mice to generate UTX-TCD P14 mice ($Utx^{-/-}$ P14 [P14$^+$LckCre$^+$$Utx^{fl/fl}$]). All CD8$^+$ T cells in these mice recognize the LCMV $GP_{33–41}$ epitope, lack expression of UTX, and co-express the congenic $Ly5^a$ (CD45.1) and $Ly5^b$ (CD45.2) alleles (Figures 2A and S3A). For WT donor controls, we used cells from $P14^+Utx^{+/+}LckCre^+$ mice that were homozygous for the $Ly5^a$ allele. Recipient mice were depleted of CD4$^+$ T cells, allowing for high viral burdens at day 35 post-infection (Figure 2B). This approach allowed us to track antiviral WT and UTX-deficient CD8$^+$ T cell responses under identical inflammatory and virological conditions.

Both WT and $Utx^{-/-}$ P14s accumulated to high frequencies in the blood by day 10 post-infection, although there were 3-fold more $Utx^{-/-}$ P14s than P14$^+$LckCre$^+$Utx$^{wt/wt}$ (WT P14) cells in the same recipients. The frequencies of both donor P14 cell populations began to decline after day 10; however, the ratio of $Utx^{-/-}$ to WT P14s steadily increased to 12-fold by day 22 and 21-fold by day 35 (Figure 2C). In the spleen, $Utx^{-/-}$ P14s showed limited contraction and were as numerous at day 35 as at day 9, whereas WT P14 cells steadily contracted during this period (Figure 2D). When compared in separate recipient mice so that the cells were not in direct competition for antigen or cytokines, $Utx^{-/-}$ P14s were significantly higher in frequency and number compared to WT (Figures S3B and S4A–S4G). These data indicate that UTX functions intrinsically within CD8$^+$ T cells to limit their abundance after infection in both lymphoid and nonlymphoid tissues.

CD4$^+$ T cell depletion is a common approach when investigating T cell exhaustion, as it replicates the defects in CD8$^+$ T cells that are observed during chronic infections in humans. We considered that UTX might make CD8$^+$ T cells dependent on CD4$^+$ T cell help during chronic infection. We performed a dual adoptive transfer without depleting CD4$^+$ T cells and found that $Utx^{-/-}$ P14s expanded 2.1-fold more than WT P14s and persisted at 3.3-fold higher frequencies at day 22 post-infection (Figure S3C). Additionally, mixed bone marrow chimera mice were generated with different ratios of WT and UTX-TCD bone marrow, resulting in mice with a polyclonal mixture of WT and $Utx^{-/-}$ T cells. At days 22–23 post-infection, the endogenous $Utx^{-/-}$ GP_{33}-tetramer$^+$CD8$^+$ T cells outnumbered their WT counterparts in chimeras established with 50:50 (WT/knockout [KO]) or 60:40 ratios of bone marrow, with more equivalent responses found only when the precursor frequency favored WT T cells by 80:20 (Figure S3D), consistent with UTX restricting CD8$^+$ T cell

expansion and survival. A single copy of *Utx* was sufficient to limit T cell responses, as *Utx* heterozygous P14 cells (*P14*$^{+}$*Utx*$^{wt/fl}$*LckCre*$^{+}$) out-expanded and were maintained at higher frequencies in the spleen than WT P14 cells in the same recipients (Figure S3E and S3F). Cumulatively, these data show that UTX limits the accumulation and persistence of virus-specific CD8^{+} T cells during chronic infection, and does so regardless of the availability of CD4 help or inter-clonal competition.

UTX restricts T cell responses and memory formation following acute LCMV infection

Consistent with earlier reports (Kaech et al., 2002; Russ et al., 2014; Yu et al., 2017), acute LCMV-Armstrong infection resulted in memory phenotype (CD44^{hi}) T cells with upregulated expression of UTX compared to naive CD8^{+} T cells (Figure S5A), suggesting that UTX might play a role in T cell memory formation. To determine whether UTX-mediated changes in CD8^{+} T cell frequency were common to acute and chronic infections, we examined primary and memory T cell responses following acute infection with LCMV-Armstrong, which was resolved by day 8 (data not shown). Compared to WT, *Utx*$^{-/-}$ P14s in the same recipients trended toward an increase in frequency in the spleen at days 8 and 43, a pattern minimally impacted by the presence or absence of host CD4^{+} T cells (Figure S5B). A greater frequency of *Utx*$^{-/-}$ P14s were CD44^{+}CD62L^{+} (central-memory phenotype) rather than CD44^{+}CD62L^{-} (effector-memory phenotype) (Figures S5C and S5D), and a higher proportion of *Utx*$^{-/-}$ memory T cells expressed interleukin (IL)-7R compared to WT (Figure S5E). Thus, UTX limits the number of central-memory phenotype T cells following acute infection, although its effects on T cell frequencies are less prominent as compared to those seen during chronic infection.

Utx$^{-/-}$ cells show evidence of resistance to apoptosis

Increases in T cell number can be achieved through enhanced cell division or decreased apoptosis. To address the effect of UTX on T cell proliferation, bromodeoxyuridine (BrdU) incorporation was assayed in co-transferred WT and *Utx*$^{-/-}$ P14s following LCMV-A22 infection (Figure 2E). Roughly 80% of both donor cells were BrdU^{+} at day 7 post-infection (Figure 2F). Similarly, Ki67 nuclear antigen staining indicated slightly fewer proliferating *Utx*$^{-/-}$ T cells, compared to WT (Figure 2G). These data suggest that UTX does not suppress CD8^{+} T cell proliferation, consistent with our earlier findings that *Utx*$^{-/-}$ CD8^{+} T cells proliferate normally to anti-CD3/CD28 stimulation *in vitro* (Cook et al., 2015).

The ratio of pro-apoptotic BIM to anti-apoptotic BCL2 can be used to indicate the relative potential of cells to undergo apoptosis (Wojciechowski et al., 2007). At day 9 post-infection, WT and *Utx*$^{-/-}$ P14s expressed similar amounts of BIM, although WT T cells expressed lower amounts of BCL2, resulting in a significantly higher BIM/BCL2 gMFI ratio for WTP14s (Figure 2H). A greater proportion of WT P14s stained positive for cleaved caspase-3 (Figure 2I) and bound annexin V than did *Utx*$^{-/-}$ P14s (Figure 2J). Cumulatively, these independent measures of cell viability imply that UTX-deficient CD8^{+} T cells are relatively protected from apoptosis, which may explain how they are maintained over time while WT T cell frequencies decline.

UTX supports the effector functions of virus-specific CD8$^+$ T cells

We examined the functional impact of UTX on antiviral CD8$^+$ T cell responses, focusing on T cell production of antiviral cytokines and their ability to function as cytolytic killers. At days 9 and 22 post-infection, splenocytes were briefly stimulated with $GP_{33–41}$ peptide followed by intracellular cytokine staining (ICCS). While the proportion of donor P14$^+$ T cells producing tumor necrosis factor (TNF) and IL-2 was similar (data not shown), fewer *Utx*$^{-/-}$ P14 T cells produced IFNγ compared to WT P14 cells at both times (Figure 3A). WT P14 cells made more IFNγ on a per cell basis than did *Utx*$^{-/-}$ P14s (Figure 3B), suggesting an intrinsic role for UTX in regulating CD8$^+$ T cell production of IFNγ. The functional avidity of the T cells (Slifka and Whitton, 2001) (i.e., their ability to make IFNγ in response to trace amounts of antigen) was not impacted by UTX, as WT and *Utx*$^{-/-}$ P14 cells from day 8 post-infection showed similar half-maximal responses (approximately 0.2–0.5 nM) when exposed to varying concentrations of $GP_{33–41}$ peptide (Figures 3C and 3D). However, the percentage of cells making IFNγ at high peptide concentrations and the amount of IFNγ made per cell (gMFI) were greatly reduced in the absence of UTX (Figures 3C and 3D). Similarly, WT and *Utx*$^{-/-}$ CD8$^+$ T cells induced by acute infection showed overlapping half-maximal responses (Figures S5F and S5G), but fewer *Utx*$^{-/-}$ memory T cells could make IFNγ and they expressed it at lower amounts on a per cell basis.

A higher percentage of WT P14 cells were granzyme B$^+$ at day 9, compared to *Utx*$^{-/-}$ P14 cells (Figure 3E), and a similar pattern held at day 22. Both WT and *Utx*$^{-/-}$ P14s could degranulate, as indicated by the migration of CD107a/b to the cell surface upon stimulation (Betts et al., 2003), although *Utx*$^{-/-}$ P14 cells showed slightly lower CD107a/b fluorescence on a per cell basis (Figure 3F). Finally, T cell antiviral activity was assessed by delivering WT or *Utx*$^{-/-}$ P14 cells to immune-deficient RAG-KO mice, followed by LCMV-A22 challenge. At day 7 post-infection, *Utx*$^{-/-}$ P14 cells outnumbered WT cells (Figure 3G), yet there was more virus in the tissues of these mice than recipients with WT P14 cells (Figures 3G and 3H). In total, these findings indicate that UTX enhances antiviral CD8$^+$ T cell effector functions during chronic infection.

UTX increases inhibitory receptor expression by CD8$^+$ T cells

During the course of persistent infection, CD8$^+$ T cells express increasing amounts and combinations of inhibitory receptors. Inhibitory receptor signaling can block proximal TCR signaling or transmit other signals that reduce T cell reactivity or lead to T cell apoptosis. To assess the effect of UTX on inhibitory receptor expression, WT and *Utx*$^{-/-}$ P14s were transferred to separate mice followed by CD4 depletion and infection with LCMV-A22. In the blood, significantly higher proportions of WT than *Utx*$^{-/-}$ P14 cells expressed PD-1, LAG-3, TIM-3, and 2B4 (Figures 4A–4D), and a similar pattern was observed in the liver and lungs of mice (Figures S4H and S4I). The difference in expression appeared as early as day 8 and was maintained through day 37 post-infection. WT P14s also showed higher expression of PD-1 and TIM-3 on a per cell basis, though LAG-3 and 2B4 levels were not impacted by UTX (Figure 4E). These differences in inhibitory receptor expression occurred despite similar virus burdens in the recipient mice (Figures 4F). These findings indicate that UTX increases the expression of inhibitory receptors that can restrain T cell numbers and activity during persistent infection.

UTX alters gene expression in virus-specific CD8$^+$ T cells

UTX can impact transcription by demethylase-dependent and demethylase-independent mechanisms that include interactions with other chromatin-modifying enzymes or transcription factors (Beyaz et al., 2017; Froimchuk et al., 2017; Shpargel et al., 2012; Shpargel et al., 2017). To determine whether UTX significantly alters gene expression patterns in CD8$^+$ T cells, WT and *Utx*$^{-/-}$ P14$^+$ CD8$^+$ T cells were fluorescence-activated cell sorted (FACS) to purity from day 21 infected mice and analyzed by RNA sequencing (RNA-seq) (Figure 5A). EdgeR analysis revealed that *Utx*$^{-/-}$ P14s showed significantly (false discovery rate [FDR] < 0.05; $\log_2$[fold change] < −1.0) decreased expression of 443 transcripts compared to WT P14s (Figure 5B; Table S1). Gene set enrichment analysis (GSEA) revealed reduced expression of granzyme and other effector genes (Pauken et al., 2016) in the absence of UTX (Figure 5C), consistent with the weak CTL-mediated protection afforded by UTX-deficient CD8$^+$ T cells (Figure 3). GOrilla Gene Ontology analysis identified *Utx*$^{-/-}$ alterations in several cell cycle and immunological pathways (Figure 5D; Table S2).

To determine which changes in mRNA expression depend on the demethylase activity of UTX, we identified loci with reduced H3K27me3 in WT compared to UTX-deficient P14 CD8$^+$ T cells. CUT&RUN is a low cell number assay for chromatin occupancy where an antibody directs micrococcal nuclease to release bound DNA for sequencing (Skene and Henikoff, 2017). H3K27me3 CUT&RUN analyses (Figure 5E; Table S3) demonstrated that most genes with reduced expression by RNA-seq quantification (purple) showed increased H3K27me3. For example, when compared to *Utx*$^{-/-}$ cells, T cells with UTX expressed several genes (*Gzma, Gzmb, Thy1*) at higher levels, and these genes had lower densities of H3K27me3 marks (Figure 5F). A smaller subset of genes demonstrated enhanced expression in the absence of UTX (green), but there was no correlation with H3K27me3 (Figure 5E; Table S3).

We performed UTX chromatin occupancy analysis (CUT&Tag) to characterize where UTX binds throughout the genome. Peaks with a significant enrichment of UTX CUT&Tag signal were mapped to the closest gene within 20 kb distance (Table S4). UTX bound to several TSSs, but also frequently bound nearby distal genic regions or elsewhere within the gene body, which may represent regulatory enhancers. Existing ATAC-seq (assay for transposase-accessible chromatin using sequencing) data from CD8$^+$ T cells at day 30 of LCMV-Clone13 infection (Beltra et al., 2020) were used to identify areas of open chromatin. The ATAC data were overlaid with H3K27ac chromatin immunoprecipitation sequencing (ChIP-seq) maps from P14 cells from day 7 LCMV-Clone13-infected mice (Yao et al., 2019) to identify putative enhancers that are active during chronic infection. Peaks of UTX binding increased based on read counts after infection (day 0 versus day 15 post-infection, Figures 5G and 5H). UTX-bound TSSs tended to have elevated associations over UTX-bound enhancers (Figure 5G versus Figure 5H) and both classes of peaks were lost in *Utx*$^{-/-}$ P14 cells (KO). Out of 2,816 UTX-bound sites, there was a comparable split between TSSs (45% of UTX peaks) and enhancers (49% of UTX peaks), with most of these enhancers (>90%) having active acetylation during chronic LCMV infection (Figure 5I).

Among genes that lost expression in *Utx*$^{-/-}$ P14 cells, 39% (82/212) were bound by UTX and showed an increase in H3K27me3 in *Utx*$^{-/-}$ cells compared to WT (Figure 5J, right). However, other UTX-dependent genes that were not directly bound by UTX (Figure 5J, left) showed similar increases in *Utx*$^{-/-}$ H3K27me3 (34%: 234/691), suggesting that H3K27me3 changes may not be attributed to direct UTX binding. The overall density of H3K27me3 reads were reduced at UTX-bound loci compared to genome-wide H3K27me3 peaks (Figures 5K and 5L). However, WT and *Utx*$^{-/-}$ P14 cells had similar low-level H3K27me3 read density at both UTX-bound TSSs and enhancers (Figures 5M and 5N).

We examined whether UTX binding correlated with enhancer chromatin in T cells at different stages of T cell exhaustion (Tex), including progenitor cells (Tex$^{prog1/2}$) that are responsive to checkpoint blockade, Tex-intermediate (Tex^{int}) cells, and terminally differentiated cells (Tex^{term}) that fail to recover function with blockade and are prone to apoptosis (Beltra et al., 2020). Based on Tex^{prog1} ATAC-seq reads, annotated enhancers demonstrated elevated open chromatin when bound by UTX (Figure 5O). The chromatin accessibility of UTX-bound enhancers increased in Tex^{int} cells (Figure 5P), implying a shift in enhancer activation as P14 cells transition to the exhausted state. UTX-bound enhancers showed evidence of heightened activation (H3K27ac levels) in Tex (Figure 5Q). Overall, UTX binding tends to not correlate with dramatic changes in H3K27 methylation but may function in enhancer activation.

We examined UCSC browser images of chromatin occupancy for several genes that were regulated by UTX (Figures S6A–S6C). Genes associated with activation and T cell effector function such as *Tnfrsf9 (4-1bb), Gzmb*, and *Cd9* lost expression and accumulated H3K27me3 in *Utx*$^{-/-}$ cells at day 15 of infection (Figure S6A). These regions were bound by UTX, which increased as the cells transitioned from naive to effector cells (Figure S6B). Active enhancers were annotated as non-TSS peaks of open chromatin (ATAC-seq of day 30 LCMV-Clone13-infected P14 cells; Beltra et al., 2020), which also overlapped H3K27ac peaks (Yao et al., 2019) from day 7 LCMV-infected mice (Figure S6C, top). These putative enhancers aligned with H3K4me1 enrichment, as identified in effector CD8$^+$ T cells from acutely infected mice (He et al., 2016). In contrast, TSSs appear as areas with enriched H3K4me3 (Figure S6C, bottom), as identified in CD8$^+$ T cells from early stages of acute infection (Shan et al., 2017). UTX binding at these genic locations closely overlapped putative active enhancers (*Tnfrsf9* and *Cd9*) or a TSS (*Gzmb*) but did not correlate with broad regions where H3K27me3 differs between WT and *Utx*$^{-/-}$ (Figure S6A). A composite of all significant changes in H3K27me3 and UTX binding with nearby gene expression results can be found in Tables S3 and S4.

A motif analysis (HOMER) of UTX-bound enhancers identified potential transcription factors that might function with UTX (Figure S6D; Table S5). These transcription factors include those induced by TCR and costimulatory molecule signaling (Jun, AP1, NFAT), BATF, a factor required for T-bet and BLIMP expression and cytokine responses (Kurachi et al., 2014), as well as T-bet and eomesodermin, which are associated with subsets of Tex^{term} or Tex^{prog} cells (McLane et al., 2019). In sum, UTX can localize to TSSs or enhancers to directly promote the expression of effector genes in CD8$^+$ T cells, although these effects appear regulated largely through H3K27me3 demethylase-independent mechanisms.

UTX demethylase activity is not required for effector CD8$^+$ T cell function during chronic infection

To assess whether demethylase activity is required for UTX to enhance the effector functions of CD8$^+$ T cells, we analyzed T cells from mice with a catalytic-dead knockin point mutation of UTX (*Utx*$^{KI/KI}$, Shpargel et al., 2017). *Utx*$^{KI/KI}$ mice given LCMV-Clone13 or LCMV-A22 infection with CD4 depletion established persistent infections with antiviral T cell numbers and T cell expression of inhibitory receptors or granzyme that were not significantly different from WT mice (Figure S7).

To more precisely define the role of UTX demethylation in CD8$^+$ T cells, WT, *Utx*$^{KI/KI}$, and *Utx*$^{-/-}$ P14$^+$ CD8$^+$ T cells with distinct congenic markers (Ly5a, Ly5b, and Thy1.1) were co-transferred into the same recipients, followed by CD4 depletion and infection with LCMV-A22 (Figures 6A and 6B). At day 8 post-infection, the frequency of *Utx*$^{-/-}$ cells was significantly greater than either WT or P14$^+$ *Utx*$^{KI/KI}$ (*Utx*$^{KI/KI}$ P14) cells, which were not significantly different between themselves (Figure 6C). T cell differentiation into functionally exhausted subsets is impacted by T-BET, EOMES, TOX, and TCF1 transcription factors, which were differentially expressed depending on UTX genotype (Figure 6D). *Utx*$^{-/-}$ cells underexpressed T-BET and overexpressed EOMES and TCF1, whereas *Utx*$^{KI/KI}$ cells were similar to WT. Notably, both *Utx*$^{-/-}$ and *Utx*$^{KI/KI}$ underexpressed TOX1, suggesting that the demethylase domain of UTX is required for its expression, although *Utx*$^{-/-}$ P14 cells did not show increases in H3K27me3 at *Tox* (Table S3). As expected from Figure 2, *Utx*$^{-/-}$ T cells overexpressed BCL2, whereas *Utx*$^{KI/KI}$ T cells showed only a modest increase. Thus, some T cell transcription factors increase in expression in the presence of UTX, such as T-BET and TOX, with TOX requiring UTX's demethylase activity for this effect. However, other transcription factors (e.g., EOMES, TCF1, BCL2) are reduced in the presence of UTX, perhaps due to UTX-dependent activation of inhibitors.

The donor cells varied in their expression of granzyme and IFNγ. As expected, a smaller fraction of the *Utx*$^{-/-}$ P14 T cells made granzyme, and their level of expression per cell was greatly reduced compared to WT (Figures 6E and 6F). *Utx*$^{KI/KI}$ P14 cells showed minimal reductions in frequency or amount of granzyme expressed, and similar patterns held when IFNγ expression was quantified (Figures 6G and 6H). Among all P14 populations, there were cells that made or did not make IFNγ upon peptide stimulation (Figure 6I). There were comparable frequencies of WT, *Utx*$^{-/-}$, and *Utx*$^{KI/KI}$ CD8$^+$ T cells among cells making IFNγ. However, a high frequency of *Utx* cells was found among the cells failing to make IFNγ, whereas few *Utx*$^{KI/KI}$ or WT cells were unable to make IFNγ. These data indicate that UTX does not require demethylase activity to allow CD8$^+$ T cells to express IFNγ.

Among T cells responding to peptide and making IFNγ, other T cell molecules (CD5, CD9, CD44, CD69) associated with T cell activation and TCR signal strength were modestly changed when UTX was absent and normal when the UTX catalytic mutant was present (Figure 6J). Among the cytokine responsive cells, PD-1 showed minimal alteration in expression, although TIM-3 and 2B4 were underexpressed when UTX was absent and largely unchanged by the UTX-KI mutation (Figure 6J).

Ly108 and CD69 co-staining can be used to distinguish Tex^{prog1}, Tex^{prog2}, Tex^{int}, and Tex^{term} subsets, which differ in terms of their responsiveness to checkpoint blockade (Beltra et al., 2020). $Utx^{-/-}$ P14 cells showed a large outgrowth of Tex^{prog1} and Tex^{prog2} subsets (Figures 6K and 6L), whereas the $Utx^{KI/KI}$ P14 cells more closely resembled WT P14 cells and were predominantly Tex^{int} cells. These data suggest that UTX advances the differentiation of $Tex^{prog1/2}$ to Tex^{int} or Tex^{term} subsets, and this process does not require its demethylase domain. Consistent with these data, UTX-bound enhancers correlate with ATAC-seq-based chromatin accessibility changes that occur across Tex^{prog1} to Tex^{int} cellular subtypes (Figures 5O and 5P).

In summary, these genetic and genomic data demonstrate that UTX functions in $CD8^+$ T cell gene regulation largely through demethylase-independent mechanisms, with UTX targeting TSSs or enhancers to induce expression. In addition to promoting effector functions and inhibitory receptor expression, UTX limits virus-specific T cell numbers and impacts whether $CD8^+$ T cells become terminally exhausted, suggesting that interference in UTX levels or UTX-interacting partners could prevent-terminal exhaustion.

DISCUSSION

T cells responding to infection differentiate into distinct lineages that are sustained across time through epigenetic processes. Multiple enzymes are involved in stabilizing T cells so that the cells can express lineage-appropriate cytokines and other molecules and persist as a differentiated pool over time. Unlike memory T cells induced by transient vaccines or acute infections, virus-specific T cells subjected to persistent virus infection undergo excessive cell death or, depending on specificity, persist in a functionally deficient, exhausted state. Epigenetic mechanisms orchestrate the transcriptional changes associated with $CD8^+$ T cell differentiation, although the roles of specific chromatin-modifying proteins in mediating these transcriptional changes are not fully understood (Henning et al., 2018; McLane et al., 2019). In this study, we identify UTX as a critical regulator of virus-specific $CD8^+$ T cell differentiation and antiviral activity during virus infection. UTX expression allowed $CD8^+$ T cells to elaborate antiviral effector activity in part by improving the transcription of effector molecules, but UTX also increased T cell expression of inhibitory receptors and was associated with reduced T cell stability during the course of infection. Genes showing UTX-dependent expression showed broad reductions in H3K27me3 levels. However, $CD8^+$ T cells expressing a demethylase-dead mutant UTX were phenotypically similar to WT, suggesting that UTX guides gene expression through demethylase-independent mechanisms, most likely by binding enhancers and TSSs of actively expressed genes and promoting their expression. These data indicate that UTX guides the size, duration, and antiviral activity of virus-specific $CD8^+$ T cells.

Multiple underlying mechanisms lead to excessive loss of virus-specific $CD8^+$ T cells during protracted infection. For example, $CD4^+$ T cells play a key role in supporting $CD8^+$ T cell responses during chronic infection, including through their expression of IL-21 and promotion of antibody responses that reduce viral burden (Elsaesser et al., 2009; Kahan et al., 2015; Yi et al., 2009). Mice depleted of $CD4^+$ T cells show exaggerated features of $CD8^+$ T cell exhaustion and virus persistence. We previously showed that UTX plays a key

role in the generation of Tfh cells and B cell responses to limit chronic infection (Cook et al., 2015). We found that WT mice generated as many virus-specific $CD8^+$ T cells as did UTX-TCD mice, although UTX-TCD mice had defective Tfh cells. In the present study, we show that when compared in the same host, WT $CD8^+$ T cells accumulated less than $Utx^{-/-}$ $CD8^+$ T cells, indicating that UTX functions intrinsically within $CD8^+$ T cells to limit their number. Additionally, $CD8^+$ T cell expression of inhibitory receptors is linked to increased senescence and apoptosis (Pauken et al., 2016). We found that UTX increases the expression of several inhibitory receptors (PD-1, LAG-3, TIM-3, and 2B4) (Figure 4), and UTX-deficient T cells appear resistant to apoptosis (Figure 2), which suggests that UTX may potentiate cell death by increasing the cell surface expression of inhibitory receptors. There are subsets of T cells that vary in their ability to be rescued by checkpoint blockade during chronic infection (Im et al., 2016; Paley et al., 2012). PD-1^{hi} T cells are terminally differentiated and cannot be rescued by PD-1-PD-L1 blockade, whereas PD-1^{int} cells respond to checkpoint blockade, proliferate, and recover antiviral function. Given that *Utx*$^{-/-}$ $CD8^+$ T cells express intermediate levels of PD-1, transient interference with UTX expression might be an approach to improve adoptive immunotherapy or to increase the proportion of exhausted $CD8^+$ T cells that can be rescued by checkpoint blockade.

Following acute infection with LCMV-Armstrong, UTX-deficient $CD8^+$ T cells formed more memory T cells, including IL-7$Ra^{hi}$$KLRG1^-$ cells (Figure S5), which is consistent with recent evidence that UTX suppresses $CD8^+$ T cell memory formation in mice following acute *Listeria monocytogenes* infection (Yamada et al., 2019). However, the impact of UTX on $CD8^+$ T cell number and responsiveness was far more dramatic when T cells were subjected to chronic infection. We surmise that the fundamental trends are similar, but ongoing antigenic stimulation draws out these differences during chronic infection. UTX-deficient T cells expressed reduced Thy1, CD9, and several other TCR-associated molecules, suggesting that the improved survival of T cells in the presence of ongoing infection may be linked to diminished TCR signaling and reduced activation-induced cell death. UTX deficiency did not reduce the functional avidity maturation of $CD8^+$ T cells, suggesting that early T cell differentiation unfolds normally in its absence; however, UTX was needed for maximal expression of IFNγ, granzymes, and immune protection against disseminated infection. Thus, UTX fine-tunes $CD8^+$ T cell responses, perhaps allowing for rapid immune defense at early stages of infection while countering the harmful effects of immune-mediated pathology after the infection has established persistence.

UTX-deficient $CD8^+$ T cells underexpressed numerous genes. Many of these, including *granzyme A, granzyme B, Thy1*, and *Cd9*, accumulated H3K27me3, suggesting that UTX may function by demethylating these loci to enable transcription. However, H3K27me3 accumulated across broad genic domains that failed to correlate with sites of UTX binding. Other loci, such as *Ifng*, showed reduced mRNA levels in $CD8^+$ T cells lacking UTX but did not show significant changes in H3K27me3. It is plausible that these loci are partly demethylated by JMJD3, resulting in residual expression in UTX-deficient T cells. UTX and JMJD3 typically operate at distinct sites, although there can be redundancy at some loci (Manna et al., 2015). Interestingly, UTX promoted inhibitory receptor expression without significantly changing its mRNA expression, suggesting that UTX affects the post-transcriptional regulation of these proteins. Finally, UTX can promote gene expression

independent of its demethylase domain by seeding pro-transcription complexes at gene promoters or enhancers (Miller et al., 2010; Shpargel et al., 2012; Wang et al., 2017; Yoo et al., 2016), which may explain why some genes show UTX-dependent increases in gene expression, yet show no alteration in H3K27me3 marks and can be activated by a catalytically dead version of UTX (Figures 5 and 6). UTX was bound to putative enhancers of many gene targets that failed to be expressed in the absence of UTX. As these enhancers become activated in P14 cells during chronic LCMV infection, UTX may guide gene expression patterns that drive T cells toward the exhausted phenotype.

In summary, our findings show that UTX modulates antiviral $CD8^+$ T cell responses at various stages of virus infection, simultaneously promoting early antiviral activity while increasing inhibitory receptor expression and reducing long-term T cell survival. A better understanding of the epigenetic landscape in exhausted T cells and the role of specific chromatin-modifying proteins may lead to the development of a new class of immunotherapy agents that reprogram T cells for durable protection.

STAR★METHODS

RESOURCE AVAILABILITY

Lead contact—Further information and requests for resources and reagents should be directed to and will be fulfilled by the Lead Contact, Jason Whitmire (jwhitmir@email.unc.edu).

Materials availability—$UTX^{fl/fl}$ and $UTX^{KI/KI}$ mice are available upon request, with standard institutional material transfer agreements and evidence of institutional approval to receive mice.

Data and code availability—All data are available within this article. RNA-sequencing, CUT&RUN-sequencing, and CUT&TAG-sequencing data have been deposited to Gene Expression Omnibus under Accession GSE143736. No new code was generated for this study.

EXPERIMENTAL MODEL AND SUBJECT DETAILS

Mice—C57BL/6 (B6), B6.$Ly5^{a/a}$ (CD45.1), and B6.*Lck-cre* mice were purchased from Jackson Laboratory (Bar harbor, Maine). $Utx^{fl/fl}$ mice were generated at UNC and backcrossed to C57BL/6 (Shpargel et al., 2012). $Utx^{KI/KI}$ mice were generated at NIDDK and then backcrossed 10 times to C57BL/6J in the Whitmire lab. UTX-TCD mice express one copy of the *Lck-cre* transgene and were generated by crossing Lck-cre-transgenic mice (Hennet et al., 1995) to $Utx^{fl/fl}$ mice. P14 TCR-transgenic mice contain $CD8^+$ T cells specific for LCMV $GP_{33–41}$ were backcrossed to B6.$Ly5^{a/a}$ mice and were maintained in a hemizygous state ($P14^{+/0}$). Both *Lck-cre*$^+$$Utx^{wt/wt}$ and *Lck-Cre*$^-$$Utx^{fl/fl}$ mice were used as WT controls, as they fail to delete the *Utx* gene. $P14^+$*Lck-cre*$^+$$Utx^{wt/wt}$ mice (WT $P14^+$) were generated by intercrossing $P14^+$*Lck-cre*$^+$ mice to $Utx^{wt/wt}$ mice. $P14^+$*Lck-cre*$^+$$UTX^{fl/fl}$ mice ($Utx^{-/-}$ $P14^+$) were generated by intercrossing $P14^+$*Lck-cre*$^+$ mice to $Utx^{fl/fl}$ mice. $Utx^{KI/KI}$ mice were intercrossed to P14 mice to generate the P14+$Utx^{KI/KI}$ mice. Congenic

P14^{+} mice were either Ly5$^{a/b}$, Ly5$^{a/a}$, or Ly5$^{b/b}$, as indicated. All experimental mice were female and hemizygous for both *P14* and *Lck-cre* transgenes. Mice were bred and housed in a facility managed by the Division of Comparative Medicine at UNC-CH. All mouse experimental procedures were approved by the University of North Carolina Institutional Animal Care and Use Committee.

Virus—Adult mice (8-10 weeks) received 2x10^{6} plaque-forming units (PFU) LCMV-A22 by intravenous tail vein injection or, where indicated, 2x10^{5} PFU LCMV-Armstrong. Stocks of LCMV were produced from BHK-21 cells after infection with plaque-purified isolates and were tested negative for mycoplasma. Virus titer in serum, liver, lung, and kidney was quantified by plaque assay on Vero cell monolayers (Ahmed et al., 1984).

Cell isolation and purification—Single-cell suspensions from spleens were prepared by physically disrupting the tissue over a 70um strainer (Corning, NY). Erythrocytes were removed from the spleen suspension using ACK lysing buffer. Blood leukocytes were isolated using heparinized capillary tubes and collected into 4% sodium citrate; cells were underlaid with Histopaque-1077, centrifuged, and the leukocytes removed from the resulting interphase. All single-cell preparations were rinsed and re-suspended in 10% RPMI media.

Cell culture—Vero cells and BHK cells were propagated in DMEM supplemented with 5% heat-inactivated FBS, penicillin, streptomycin, and fungizone.

METHOD DETAILS

Adoptive transfers—Splenocytes were isolated from WT and *Utx*$^{-/-}$ P14 TCR transgenic mice, and the frequency of Vα2^{+}Vβ8.1/2^{+}CD8^{+} T cells was determined by flow cytometry. In some experiments, 2x10^{3} WT or *Utx*$^{-/-}$ P14^{+}CD8^{+} T cells were injected via intravenous tail-vein injection into separate C57BL/6 mice. In co-transfer experiments, 1x10^{3} WT and 1x10^{3} *Utx*$^{-/-}$ P14s were mixed and co-transferred into the same recipients; the donor cells expressed different congenic markers (CD45.1 (Ly5^{a}) versus CD45.2 (Ly5^{b})), allowing them to be distinguished from each other and host cells by surface staining and flow cytometry. Donor cells were allowed to engraft for 5-7 days prior to LCMV infection. In some cases, CD4 T cells were depleted before infection by intraperitoneal injection of 75ug GK1.5 on days −3 and −2.

Flow cytometry and intracellular staining—Surface staining of splenocytes and peripheral blood lymphocytes was performed directly *ex vivo*. Degranulation was assessed by surface expression of CD107a and CD107b. Splenocytes were incubated (37°C at 8% CO_2) for 1 hour with LCMV peptide $GP_{33–41}$ and antibody to CD107a/b followed by addition of Monensin and additional 4-hour incubation (Betts et al., 2003). Intracellular staining for Granzyme B was performed using the True-Nuclear Transcription Factor Buffer Set. Intracellular staining for Ki67 was performed using the FoxP3 Fix/Perm Buffer Set. Cytokine production was assessed by intracellular cytokine staining for IL-2, TNF, and IFNγ following a 5 hour stimulation with $GP_{33–41}$ peptide in the presence of brefeldin A. Samples were analyzed by flow cytometry using a FACS-Calibur or LSR II (BD Biosciences), and FACS plots generated using FlowJo software.

Mixed bone marrow chimeras—Donor bone marrow was harvested from the femurs of WT and UTX-TCD Ly5a+ non-transgenic mice. Red blood cells were lysed using ACK Lysis Buffer, followed by trypan blue counting. Donor cells were mixed to obtain the desired WT:UTX-TCD ratio. Recipient C57BL/6 mice were exposed to 600 Rads then another dose of 700 Rads 4 hours later. Bone marrow cells were transferred intravenously into the irradiated mice immediately after the second radiation dose. Mice were allowed to reconstitute for 10-weeks prior to infection.

PCR genotyping—Tail DNA was isolated using a DNeasy isolation kit. Oligonucleotide primers were custom-synthesized by Eurofins Genomics. PCR amplification of DNA fragments (200- 400 bp) was performed with the specific primers and Taq DNA polymerase. General PCR conditions were: 95°C, 5 minutes; [95°C for 30 s; 55-60°C for 30 s; 72°C for 90 s] x 35 cycles; 72°C for 5 minutes. PCR products were run on a 2% agarose gel and visualized by ethidium bromide staining.

RNA-seq, CUT&RUN, and CUT&Tag—$2x10^3$ $P14^+CD8^+$ T cells were transferred to separate C57BL/6 recipient mice. $CD4^+$ T cells were depleted (75mg of GK 1.5 Ab on days −3, −2) in the recipients prior to LCMV-A22 infection. Spleens were harvested from 3-4 mice at day 15 post-infection for CUT&RUN or CUT&Tag analyses or day 21 post-infection for RNA-seq. Donor P14s were then sorted to > 97% purity using a FACSAria-II flow cytometer at the UNC flow cytometry core facility. RNA was extracted from ~10^5 sorted cells using TRIZOL reagent, followed by mRNA purification and adaptor ligation using the KAPA mRNA HyperPrep Kit (KK8580). Sequencing was performed on an Illumina HiSeq4000 at the Duke Center for Genomic and Computational Biology. The Genome Analyzer Pipeline Software was used to perform the early data analysis, including base calling and demultiplexing of the barcodes. Reads were then aligned to the mouse (mm9) genome using open source TopHat 2.0.9. Genic reads were counted using HTSeq-count. EdgeR was used to identify significant differences between datasets (FDR < 0.05) and generate logCPM values that were used to generate scatterplots.

CUT&RUN was performed on ~10^5 sorted P14 donor cells as described (Skene et al., 2018). Briefly, $P14^+$ $CD8^+$ T cells were bound to Concanavalin A beads, permeabilized with digitonin, and incubated with H3K27me3 antibody (Cell Signaling 9733S: used at 1:100) overnight at 4 degrees on a nutator. The following day, protein A fused micrococcal nuclease (700 ng/ml) was incubated to bind H3K27me3 sites and digestion was allowed to proceed for 30 minutes at 4 degrees followed by a 10 minute incubation at 37 degrees to release CUT&RUN fragments. DNA was purified by phenol chloroform extraction with ethanol precipitation and KAPA dual index adapters (KK8722) were ligated to DNA with the KAPA HyperPrep Kit (KK8504) for paired-end sequencing on the Nextseq 500 (Duke Center for Genomic and Computational Biology). CUT&RUN alignment to the mm9 genome was performed using Bowtie2 and H3K27me3 peaks called with MACS2 and hidden Domains (Starmer and Magnuson, 2016; Zhang et al., 2008). Read counts at peaks of H3K27me3 enrichment were quantified with deepTools (Ramírez et al., 2016) and edgeR identified significant (FDR < 0.05) changes in H3K27me3.

CUT&Tag was performed on ~10^5 sorted WT or *Utx*$^{-/-}$ P14 donor cells before recipient transfer (D0) or 15 days following transfer, CD4 depletion, and LCMV-A22 infection (D15). P14$^+$ CD8$^+$ T cells were bound to Concanavalin A beads, permeabilized with digitonin, and incubated with UTX antibody (Cell Signaling 33510S: used at 1:100). A secondary antibody (Guinea Pig anti-Rabbit IgG, Fisher Scientific NBP172763, 1:100) was incubated to increase antibody enrichment at UTX bound sites. Protein A fused Tn5 transposase (pA-Tn5) was expressed from the 3XFlag-pA-Tn5-FI construct (Addgene plasmid 124601) and purified as described (Kaya-Okur et al., 2019) by the University of North Carolina Protein Production Core. Adapters were ligated to the pA-Tn5 as described (Kaya-Okur et al., 2019). PA-Tn5 was incubated with the antibody bound digitonin permeabilized P14 cells and tagmentation was allowed to proceed for 1 hour at 37 degrees. DNA was extracted, purified, and dual index oligos (Buenrostro et al., 2015) amplified CUT&Tag libraries with NEBNext HiFi 2 × PCR Master mix (New England BioLabs: M0541L). Libraries were purified with KAPA Pure Beads (KK8000) for paired-end sequencing on the NovaSeq 6000 (Duke Center for Genomic and Computational Biology). CUT&Tag alignment to the mouse mm9 or *E. coli* genome was performed using Bowtie2, mm9 UTX peaks were called with MACS2 broad function (Zhang et al., 2008), and peaks with RPKM > 1 were kept for analysis. Unique read counts at peaks of UTX enrichment were quantified with deepTools (Ramírez et al., 2016), normalization factors relative to *E. coli* read counts were generated as described (Kaya-Okur et al., 2019 and https://github.com/Henikoff/Cut-and-Run/blob/master/spike_in_calibration.csh), and edgeR identified significant (FDR < 0.05) enrichment of D15 WT P14 reads compared to either D0 WT or D15 *Utx*$^{-/-}$ P14 samples based on the *E. coli* normalization factors.

Genomic analysis and data deposition—Significant UTX peaks (D15 WT P14 enriched relative to D0 WT or D15 *Utx*$^{-/-}$) and significantly elevated H3K27me3 peaks (D15 *Utx*$^{-/-}$ enriched relative to D15 WT) were mapped to the closest upstream or downstream gene using BEDTools closest (Quinlan and Hall, 2010). Genes within 20 kilobases of UTX or H3K27me3 peaks were considered direct targets of action. BEDTools intersect identified peaks that overlap genic transcription start sites (TSSs, +/− 500 bases). Enhancers were identified based on existing ATAC-seq data (GEO: GSE149877) generated from P14 donor cells following 30 days of recipient infection with LCMV Clone 13 (Beltra et al., 2020). In these data, P14 cells were flow sorted into exhausted progenitor 1 (Tex^{prog1}: Ly108+ CD69+), progenitor 2 (Tex^{prog2}: Ly108+ CD69−), intermediate exhausted (Tex^{int}: Ly108− CD69−), and terminally exhausted (Tex^{term}: Ly108− CD69+) states. ATAC-seq reads from these samples were remapped to mm9 using Bowtie2 and peaks called with MACS2 broad function (Zhang et al., 2008). Read counts at peaks of ATAC-seq enrichment were quantified with deepTools and retained with RPKM > 1. Tex^{prog1}, Tex^{prog2}, and merged ATAC-seq peaks were compiled, and peaks of open chromatin that do not overlap TSSs (+/− 500 base pairs based on BEDTools intersect) established a set of putative enhancers that may be utilized in early stages of chronic LCMV infection. Enhancer activation status was generated from existing H3K27ac ChIP-seq datasets (GSE119941) from progenitor (Blimp1−) or terminally exhausted (Blimp1+) P14 donor cells following 7 days of recipient infection with LCMV Clone 13 (Yao et al., 2019). Similar to ATAC-seq data, H3K27ac reads were remapped to mm9 and peaks of enrichment were called with

MACS2 and retained with RPKM > 1. BEDTools intersect identified active enhancers as putative enhancers peaks that overlapped H3K27ac peaks. UTX peaks were intersected with these datasets to identify bound enhancers and activation status. Profiles of UTX, H3K27me3, ATAC-seq, and H3K27ac read coverage at UTX peaks were generated with deepTools computeMatrix and plotProfile functions based on BED files of UTX peaks and Bigwig files of read coverage (generated through deepTools bamCoverage function ignoring duplicate reads). The HOMER find-MotifsGenome.pl program was utilized to identify transcription factor sequence motif enrichment at UTX bound enhancers relative to unbound enhancer control regions (Heinz et al., 2010). To validate enhancers, existing H3K4me1 ChIP-seq data obtained from $P14^{+}CD8^{+}KLRG1^{+}CD127^{lo}$ cells at 8 days post LCMV-Armstrong infection (GSE76029; He et al., 2016) were remapped mm9 and Bigwig tracks were generated for comparison to UTX peaks locations (Figure S6C). We utilized remapped Bigwig tracks from existing H3K4me3 ChIP-seq obtained from $P14^{+}CD8^{+}KLRG1^{+}CD127^{lo}$ cells at 4 days post LCMV-Armstrong infection (GSE81887; Shan et al., 2017) to illustrate enrichment at TSSs (Figure S6C). All sequencing data were generated in this study were deposited in GEO under accession number GSE143736.

T cell apoptosis—Splenocytes were collected at day 9 post-infection and cultured directly *ex vivo* for 5 hours in RPMI supplemented with 10% heat-inactivated FBS. T cell apoptosis was assessed by intracellular staining for cleaved caspase3 and surface staining for annexin-V binding.

T cell proliferation *in vivo*—Control and infected mice were given 2mg bromodeoxyuridine (BrdU) by intraperitoneal injections at days 4, 5, and 6 post-infection. Mice were also given BrdU in drinking water (0.8mg/ml) at days 4-7. Spleens were harvested at day 7 post-infection and cells stained with anti-BrdU to identify nuclear DNA with incorporated BrdU.

QUANTIFICATION AND STATISTICAL ANALYSIS

Parametric tests were conducted using unpaired two-tailed Student's t test for two groups or one-way analysis of variance (ANOVA) with Bonferroni multiple comparison test for more than two groups. When data were not normally distributed, non-parametric tests were used (Mann-Whitney U test for two groups, Kruskal-Wallis with Dunn's multiple comparison test for more than two groups). Statistical analyses were performed using Prism software (https://www.graphpad.com). All graphs are presented as mean data ± SEM. Statistical significance was determined using an unpaired Student's t test for single transfer experiments or paired Student's t test for co-transfer experiments. Differences were considered significant when $p < 0.05$ (*); < 0.01 (**); < 0.001 (***); < 0.0001 (****). EdgeR was used to identify significant differences between datasets (FDR < 0.05) and generate RPKM values for RNA-seq data.

Supplementary Material

Refer to Web version on PubMed Central for supplementary material.

ACKNOWLEDGMENTS

The authors greatly appreciate the availability of tetramers from the NIH Tetramer Core Facility at Emory University and the protein A fused micrococcal nuclease provided by the Steven Henikoff laboratory. We also benefited from the helpful services provided by the UNC flow cytometry core facility, which is supported by NCI Center Core Support Grant (5P30CA016086) and North Carolina Biotech Center Institutional Support Grant (2012-IDG-1006). This work was supported by NIH grants R01AI138337, R01AI143894, R01AI131685, and R21AI117575 to J.K.W., as well as by seed funding from North Carolina TraCS Translational Team Science Award (TTSA004P2). K.B.S. was supported by NIH awards 1R03DE027101 and 1R56DE028553; J.S. and T.M. were supported by NIH award R01GM10974. The graphical abstract was created using BioRender.

REFERENCES

Agger K, Cloos PA, Christensen J, Pasini D, Rose S, Rappsilber J, Issaeva I, Canaani E, Salcini AE, and Helin K (2007). UTX and JMJD3 are histone H3K27 demethylases involved in *HOX* gene regulation and development. Nature 449, 731–734. [PubMed: 17713478]

Ahmed R, Salmi A, Butler LD, Chiller JM, and Oldstone MB (1984). Selection of genetic variants of lymphocytic choriomeningitis virus in spleens of persistently infected mice. Role in suppression of cytotoxic T lymphocyte response and viral persistence. J. Exp. Med 160, 521–540. [PubMed: 6332167]

Bally AP, Austin JW, and Boss JM (2016). Genetic and epigenetic regulation of PD-1 expression. J. Immunol 196, 2431–2437. [PubMed: 26945088]

Barber DL, Wherry EJ, Masopust D, Zhu B, Allison JP, Sharpe AH, Freeman GJ, and Ahmed R (2006). Restoring function in exhausted CD8 T cells during chronic viral infection. Nature 439, 682–687. [PubMed: 16382236]

Beltra JC, Manne S, Abdel-Hakeem MS, Kurachi M, Giles JR, Chen Z, Casella V, Ngiow SF, Khan O, Huang YJ, et al. (2020). Developmental relationships of four exhausted $CD8^+$ T cell subsets reveals underlying transcriptional and epigenetic landscape control mechanisms. Immunity 52, 825–841.e8. [PubMed: 32396847]

Betts MR, Brenchley JM, Price DA, De Rosa SC, Douek DC, Roederer M, and Koup RA (2003). Sensitive and viable identification of antigen-specific $CD8^+$ T cells by a flow cytometric assay for degranulation. J. Immunol. Methods 281, 65–78. [PubMed: 14580882]

Beyaz S, Kim JH, Pinello L, Xifaras ME, Hu Y, Huang J, Kerenyi MA, Das PP, Barnitz RA, Herault A, et al. (2017). The histone demethylase UTX regulates the lineage-specific epigenetic program of invariant natural killer T cells. Nat. Immunol 18, 184–195. [PubMed: 27992400]

Blackburn SD, Shin H, Haining WN, Zou T, Workman CJ, Polley A, Betts MR, Freeman GJ, Vignali DA, and Wherry EJ (2009). Coregulation of $CD8^+$ T cell exhaustion by multiple inhibitory receptors during chronic viral infection. Nat. Immunol 10, 29–37. [PubMed: 19043418]

Buenrostro JD, Wu B, Litzenburger UM, Ruff D, Gonzales ML, Snyder MP, Chang HY, and Greenleaf WJ (2015). Single-cell chromatin accessibility reveals principles of regulatory variation. Nature 523, 486–490. [PubMed: 26083756]

Cacciari E, Masi M, Fantini MP, Licastro F, Cicognani A, Pirazzoli P, Villa MP, Specchia F, Forabosco A, Franceschi C, and Martoni L (1981). Serum immunoglobulins and lymphocyte subpopulations derangement in Turner's syndrome. J. Immunogenet 8, 337–344. [PubMed: 7299139]

Cook KD, Shpargel KB, Starmer J, Whitfield-Larry F, Conley B, Allard DE, Rager JE, Fry RC, Davenport ML, Magnuson T, et al. (2015). T follicular helper cell-dependent clearance of a persistent virus infection requires T cell expression of the histone demethylase UTX. Immunity 43, 703–714. [PubMed: 26431949]

Dalgliesh GL, Furge K, Greenman C, Chen L, Bignell G, Butler A, Davies H, Edkins S, Hardy C, Latimer C, et al. (2010). Systematic sequencing of renal carcinoma reveals inactivation of histone modifying genes. Nature 463, 360–363. [PubMed: 20054297]

Elsaesser H, Sauer K, and Brooks DG (2009). IL-21 is required to control chronic viral infection. Science 324, 1569–1572. [PubMed: 19423777]

Froimchuk E, Jang Y, and Ge K (2017). Histone H3 lysine 4 methyltransferase KMT2D. Gene 627, 337–342. [PubMed: 28669924]

Ghoneim HE, Fan Y, Moustaki A, Abdelsamed HA, Dash P, Dogra P, Carter R, Awad W, Neale G, Thomas PG, and Youngblood B (2017). De novo epigenetic programs inhibit PD-1 blockade-mediated T cell rejuvenation. Cell 170, 142–157.e19. [PubMed: 28648661]

Gray SM, Amezquita RA, Guan T, Kleinstein SH, and Kaech SM (2017). Polycomb repressive complex 2-mediated chromatin repression guides effector $CD8^+$ T cell terminal differentiation and loss of multipotency. Immunity 46, 596–608. [PubMed: 28410989]

Greenfield A, Carrel L, Pennisi D, Philippe C, Quaderi N, Siggers P, Steiner K, Tam PP, Monaco AP, Willard HF, and Koopman P (1998). The UTX gene escapes X inactivation in mice and humans. Hum. Mol. Genet 7, 737–742. [PubMed: 9499428]

He B, Xing S, Chen C, Gao P, Teng L, Shan Q, Gullicksrud JA, Martin MD, Yu S, Harty JT, et al. (2016). $CD8^+$ T cells utilize highly dynamic enhancer repertoires and regulatory circuitry in response to infections. Immunity 45, 1341–1354. [PubMed: 27986453]

Heinz S, Benner C, Spann N, Bertolino E, Lin YC, Laslo P, Cheng JX, Murre C, Singh H, and Glass CK (2010). Simple combinations of lineage-determining transcription factors prime *cis*-regulatory elements required for macrophage and B cell identities. Mol. Cell 38, 576–589. [PubMed: 20513432]

Hennet T, Hagen FK, Tabak LA, and Marth JD (1995). T-cell-specific deletion of a polypeptide *N*-acetylgalactosaminyl-transferase gene by site-directed recombination. Proc. Natl. Acad. Sci. USA 92, 12070–12074. [PubMed: 8618846]

Henning AN, Roychoudhuri R, and Restifo NP (2018). Epigenetic control of $CD8^+$ T cell differentiation. Nat. Rev. Immunol 18, 340–356. [PubMed: 29379213]

Im SJ, Hashimoto M, Gerner MY, Lee J, Kissick HT, Burger MC, Shan Q, Hale JS, Lee J, Nasti TH, et al. (2016). Defining $CD8^+$ T cells that provide the proliferative burst after PD-1 therapy. Nature 537, 417–421. [PubMed: 27501248]

Jensen K, Petersen PH, Nielsen EL, Dahl G, and Nielsen J (1976). Serum immunoglobulin M, G, and A concentration levels in Turner's syndrome compared with normal women and men. Hum. Genet 31, 329–334. [PubMed: 955627]

Jin C, Li J, Green CD, Yu X, Tang X, Han D, Xian B, Wang D, Huang X, Cao X, et al. (2011). Histone demethylase UTX-1 regulates *C. elegans* life span by targeting the insulin/IGF-1 signaling pathway. Cell Metab. 14, 161–172. [PubMed: 21803287]

Kaech SM, Hemby S, Kersh E, and Ahmed R (2002). Molecular and functional profiling of memory CD8 T cell differentiation. Cell 111, 837–851. [PubMed: 12526810]

Kahan SM, Wherry EJ, and Zajac AJ (2015). T cell exhaustion during persistent viral infections. Virology 479–480, 180–193.

Kaya-Okur HS, Wu SJ, Codomo CA, Pledger ES, Bryson TD, Henikoff JG, Ahmad K, and Henikoff S (2019). CUT&Tag for efficient epigenomic profiling of small samples and single cells. Nat. Commun 10, 1930. [PubMed: 31036827]

Kurachi M, Barnitz RA, Yosef N, Odorizzi PM, DiIorio MA, Lemieux ME, Yates K, Godec J, Klatt MG, Regev A, et al. (2014). The transcription factor BATF operates as an essential differentiation checkpoint in early effector $CD8^+$ T cells. Nat. Immunol 15, 373–383. [PubMed: 24584090]

Lan F, Bayliss PE, Rinn JL, Whetstine JR, Wang JK, Chen S, Iwase S, Alpatov R, Issaeva I, Canaani E, et al. (2007). A histone H3 lysine 27 demethylase regulates animal posterior development. Nature 449, 689–694. [PubMed: 17851529]

Lee S, Lee JW, and Lee SK (2012). UTX, a histone H3-lysine 27 demethylase, acts as a critical switch to activate the cardiac developmental program. Dev. Cell 22, 25–37. [PubMed: 22192413]

Lu P, Youngblood BA, Austin JW, Mohammed AU, Butler R, Ahmed R, and Boss JM (2014). Blimp-1 represses CD8 T cell expression of PD-1 using a feed-forward transcriptional circuit during acute viral infection. J. Exp. Med 211, 515–527. [PubMed: 24590765]

Manna S, Kim JK, Baugé C, Cam M, Zhao Y, Shetty J, Vacchio MS, Castro E, Tran B, Tessarollo L, and Bosselut R (2015). Histone H3 lysine 27 demethylases Jmjd3 and Utx are required for T-cell differentiation. Nat. Commun 6, 8152. [PubMed: 26328764]

McLane LM, Abdel-Hakeem MS, and Wherry EJ (2019). CD8 T cell exhaustion during chronic viral infection and cancer. Annu. Rev. Immunol 37, 457–495. [PubMed: 30676822]

Miller SA, Mohn SE, and Weinmann AS (2010). Jmjd3 and UTX play a demethylase-independent role in chromatin remodeling to regulate T-box family member-dependent gene expression. Mol. Cell 40, 594–605. [PubMed: 21095589]

Mock M, Markert UR, Vogelsang H, and Jäger L (2000). Selective T-cell deficiency in Turner's syndrome. J. Investig. Allergol. Clin. Immunol 10, 312–313.

Paley MA, Kroy DC, Odorizzi PM, Johnnidis JB, Dolfi DV, Barnett BE, Bikoff EK, Robertson EJ, Lauer GM, Reiner SL, and Wherry EJ (2012). Progenitor and terminal subsets of $CD8^+$ T cells cooperate to contain chronic viral infection. Science 338, 1220–1225. [PubMed: 23197535]

Pauken KE, Sammons MA, Odorizzi PM, Manne S, Godec J, Khan O, Drake AM, Chen Z, Sen DR, Kurachi M, et al. (2016). Epigenetic stability of exhausted T cells limits durability of reinvigoration by PD-1 blockade. Science 354, 1160–1165. [PubMed: 27789795]

Quinlan AR, and Hall IM (2010). BEDTools: a flexible suite of utilities for comparing genomic features. Bioinformatics 26, 841–842. [PubMed: 20110278]

Ramírez F, Ryan DP, Grüning B, Bhardwaj V, Kilpert F, Richter AS, Heyne S, Dündar F, and Manke T (2016). deepTools2: A next generation web server for deep-sequencing data analysis. Nucleic Acids Res. 44 (W1), W160–W165. [PubMed: 27079975]

Russ BE, Olshanksy M, Smallwood HS, Li J, Denton AE, Prier JE, Stock AT, Croom HA, Cullen JG, Nguyen ML, et al. (2014). Distinct epigenetic signatures delineate transcriptional programs during virus-specific $CD8^+$ T cell differentiation. Immunity 41, 853–865. [PubMed: 25517617]

Scott-Browne JP, López-Moyado IF, Trifari S, Wong V, Chavez L, Rao A, and Pereira RM (2016). Dynamic changes in chromatin accessibility occur in $CD8^+$ T cells responding to viral infection. Immunity 45, 1327–1340. [PubMed: 27939672]

Sen DR, Kaminski J, Barnitz RA, Kurachi M, Gerdemann U, Yates KB, Tsao HW, Godec J, LaFleur MW, Brown FD, et al. (2016). The epigenetic landscape of T cell exhaustion. Science 354, 1165–1169. [PubMed: 27789799]

Shan Q, Zeng Z, Xing S, Li F, Hartwig SM, Gullicksrud JA, Kurup SP, Van Braeckel-Budimir N, Su Y, Martin MD, et al. (2017). The transcription factor Runx3 guards cytotoxic $CD8^+$ effector T cells against deviation towards follicular helper T cell lineage. Nat. Immunol 18, 931–939. [PubMed: 28604718]

Shpargel KB, Sengoku T, Yokoyama S, and Magnuson T (2012). UTX and UTY demonstrate histone demethylase-independent function in mouse embryonic development. PLoS Genet. 8, e1002964. [PubMed: 23028370]

Shpargel KB, Starmer J, Wang C, Ge K, and Magnuson T (2017). UTX-guided neural crest function underlies craniofacial features of Kabuki syndrome. Proc. Natl. Acad. Sci. USA 114, E9046–E9055. [PubMed: 29073101]

Shpargel KB, Mangini CL, Xie G, Ge K, and Magnuson T (2020). The KMT2D Kabuki syndrome histone methylase controls neural crest cell differentiation and facial morphology. Development 147, dev187997. [PubMed: 32541010]

Skene PJ, and Henikoff S (2017). An efficient targeted nuclease strategy for high-resolution mapping of DNA binding sites. eLife 6, e21856. [PubMed: 28079019]

Skene PJ, Henikoff JG, and Henikoff S (2018). Targeted in situ genome-wide profiling with high efficiency for low cell numbers. Nat. Protoc 13, 1006–1019. [PubMed: 29651053]

Slifka MK, and Whitton JL (2001). Functional avidity maturation of $CD8^+$ T cells without selection of higher affinity TCR. Nat. Immunol 2, 711–717. [PubMed: 11477407]

Starmer J, and Magnuson T (2016). Detecting broad domains and narrow peaks in ChIP-seq data with hiddenDomains. BMC Bioinformatics 17, 144. [PubMed: 27009150]

Thrasher BJ, Hong LK, Whitmire JK, and Su MA (2016). Epigenetic dysfunction in Turner syndrome immune cells. Curr. Allergy Asthma Rep 16, 36. [PubMed: 27039394]

Virgin HW, Wherry EJ, and Ahmed R (2009). Redefining chronic viral infection. Cell 138, 30–50. [PubMed: 19596234]

Wang SP, Tang Z, Chen CW, Shimada M, Koche RP, Wang LH, Nakadai T, Chramiec A, Krivtsov AV, Armstrong SA, and Roeder RG (2017). A UTX-MLL4-p300 transcriptional regulatory network coordinately shapes active enhancer landscapes for eliciting transcription. Mol. Cell 67, 308–321.e6. [PubMed: 28732206]

Wherry EJ, and Kurachi M (2015). Molecular and cellular insights into T cell exhaustion. Nat. Rev. Immunol 15, 486–499. [PubMed: 26205583]

Wherry EJ, Ha SJ, Kaech SM, Haining WN, Sarkar S, Kalia V, Subramaniam S, Blattman JN, Barber DL, and Ahmed R (2007). Molecular signature of $CD8^+$ T cell exhaustion during chronic viral infection. Immunity 27, 670–684. [PubMed: 17950003]

Whitmire JK, Eam B, Benning N, and Whitton JL (2007). Direct interferon-γ signaling dramatically enhances $CD4^+$ and $CD8^+$ T cell memory. J. Immunol 179, 1190–1197. [PubMed: 17617612]

Wojciechowski S, Tripathi P, Bourdeau T, Acero L, Grimes HL, Katz JD, Finkelman FD, and Hildeman DA (2007). Bim/Bcl-2 balance is critical for maintaining naive and memory T cell homeostasis. J. Exp. Med 204, 1665–1675. [PubMed: 17591857]

Yamada T, Nabe S, Toriyama K, Suzuki J, Inoue K, Imai Y, Shiraishi A, Takenaka K, Yasukawa M, and Yamashita M (2019). Histone H3K27 demethylase negatively controls the memory formation of antigen-stimulated $CD8^+$ T cells. J. Immunol 202, 1088–1098. [PubMed: 30626691]

Yang XP, Jiang K, Hirahara K, Vahedi G, Afzali B, Sciume G, Bonelli M, Sun HW, Jankovic D, Kanno Y, et al. (2015). EZH2 is crucial for both differentiation of regulatory T cells and T effector cell expansion. Sci. Rep 5, 10643. [PubMed: 26090605]

Yao C, Sun HW, Lacey NE, Ji Y, Moseman EA, Shih HY, Heuston EF, Kirby M, Anderson S, Cheng J, et al. (2019). Single-cell RNA-seq reveals TOX as a key regulator of $CD8^+$ T cell persistence in chronic infection. Nat. Immunol 20, 890–901. [PubMed: 31209400]

Yi JS, Du M, and Zajac AJ (2009).A vital role for interleukin-21 in the control of a chronic viral infection. Science 324, 1572–1576. [PubMed: 19443735]

Yoo KH, Oh S, Kang K, Wang C, Robinson GW, Ge K, and Hennighausen L (2016). Histone demethylase KDM6A controls the mammary luminal lineage through enzyme-independent mechanisms. Mol. Cell. Biol 36, 2108–2120. [PubMed: 27215382]

Youngblood B, Oestreich KJ, Ha SJ, Duraiswamy J, Akondy RS, West EE, Wei Z, Lu P, Austin JW, Riley JL, et al. (2011). Chronic virus infection enforces demethylation of the locus that encodes PD-1 in antigen-specific $CD8^+$ T cells. Immunity 35, 400–412. [PubMed: 21943489]

Yu B, Zhang K, Milner JJ, Toma C, Chen R, Scott-Browne JP, Pereira RM, Crotty S, Chang JT, Pipkin ME, et al. (2017). Epigenetic landscapes reveal transcription factors that regulate $CD8^+$ T cell differentiation. Nat. Immunol 18, 573–582. [PubMed: 28288100]

Zhang Y, Liu T, Meyer CA, Eeckhoute J, Johnson DS, Bernstein BE, Nusbaum C, Myers RM, Brown M, Li W, and Liu XS (2008). Model-based analysis of ChIP-Seq (MACS). Genome Biol. 9, R137. [PubMed: 18798982]

Zhang F, Zhou X, DiSpirito JR, Wang C, Wang Y, and Shen H (2014). Epigenetic manipulation restores functions of defective $CD8^+$ T cells from chronic viral infection. Mol. Ther 22, 1698–1706. [PubMed: 24861055]

Highlights

- UTX promotes $CD8^+$ T cell-mediated antiviral defenses
- UTX increases inhibitory receptor expression and reduces T cell longevity
- UTX does not require its H3K27me3 demethylase function to promote gene expression

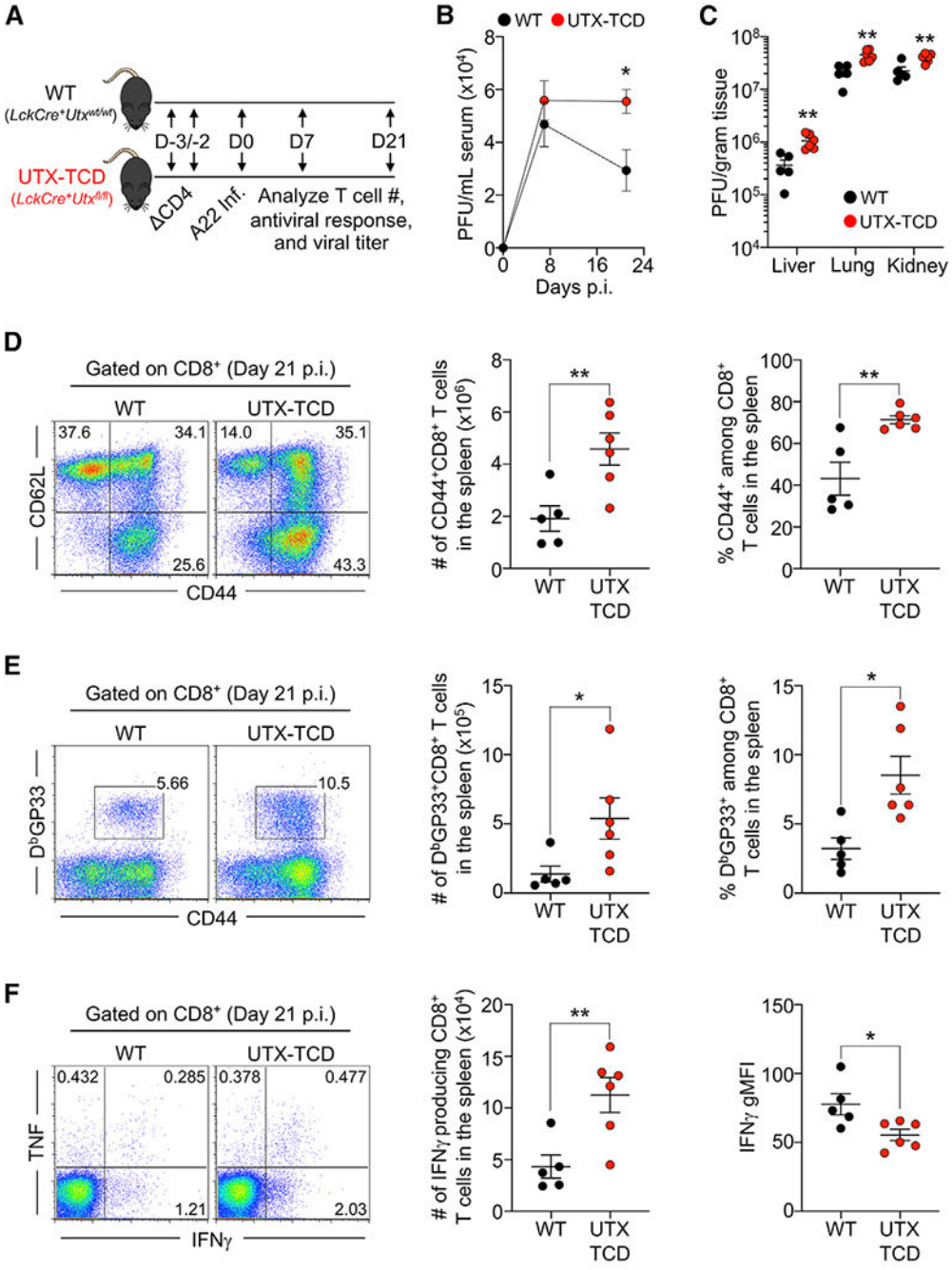

Figure 1. UTX-deficient CD8$^+$ T cells fail to control disseminated virus infection

(A) Approach: WT and UTX-TCD mice were depleted of CD4$^+$ T cells followed by LCMV-A22 infection. The contribution of UTX to CD8$^+$ T cell-dependent immune control of infection was assessed at day 21 post-infection.

(B and C) Titers of infectious virus in sera (B) and in livers, lungs, and kidneys (C) at day 21 post-infection.

(D) Dot plots show CD8$^+$ T cell expression of CD44 and CD62L, and the graphs show the number of CD44^{hi} T cells in the spleen or their percentage among CD8$^+$ T cells at day 21.

(E) Dot plots show examples of $CD8^+CD44^{hi}$ T cells bound to D^bGP33 tetramer, and the graphs show the number of D^bGP33^+ T cells per spleen or their percentage among splenic $CD8^+$ T cells.

(F) Dot plot shows $CD8^+$ T cells and their expression of IFNγ and TNF following *ex vivo* stimulation with $GP_{33–41}$ peptide; the graphs depict the total number of $IFN\gamma^+CD8^+$ T cells per spleen or the gMFI of IFNγ among IFNγ-producing $CD8^+$ T cells.

Data were combined from two independent experiments with 5–6 mice per group. Error bars display mean ± SEM. Significance was determined using an unpaired Student's t test (*$p < 0.05$, **$p < 0.01$).

See also Figures S1 and S2.

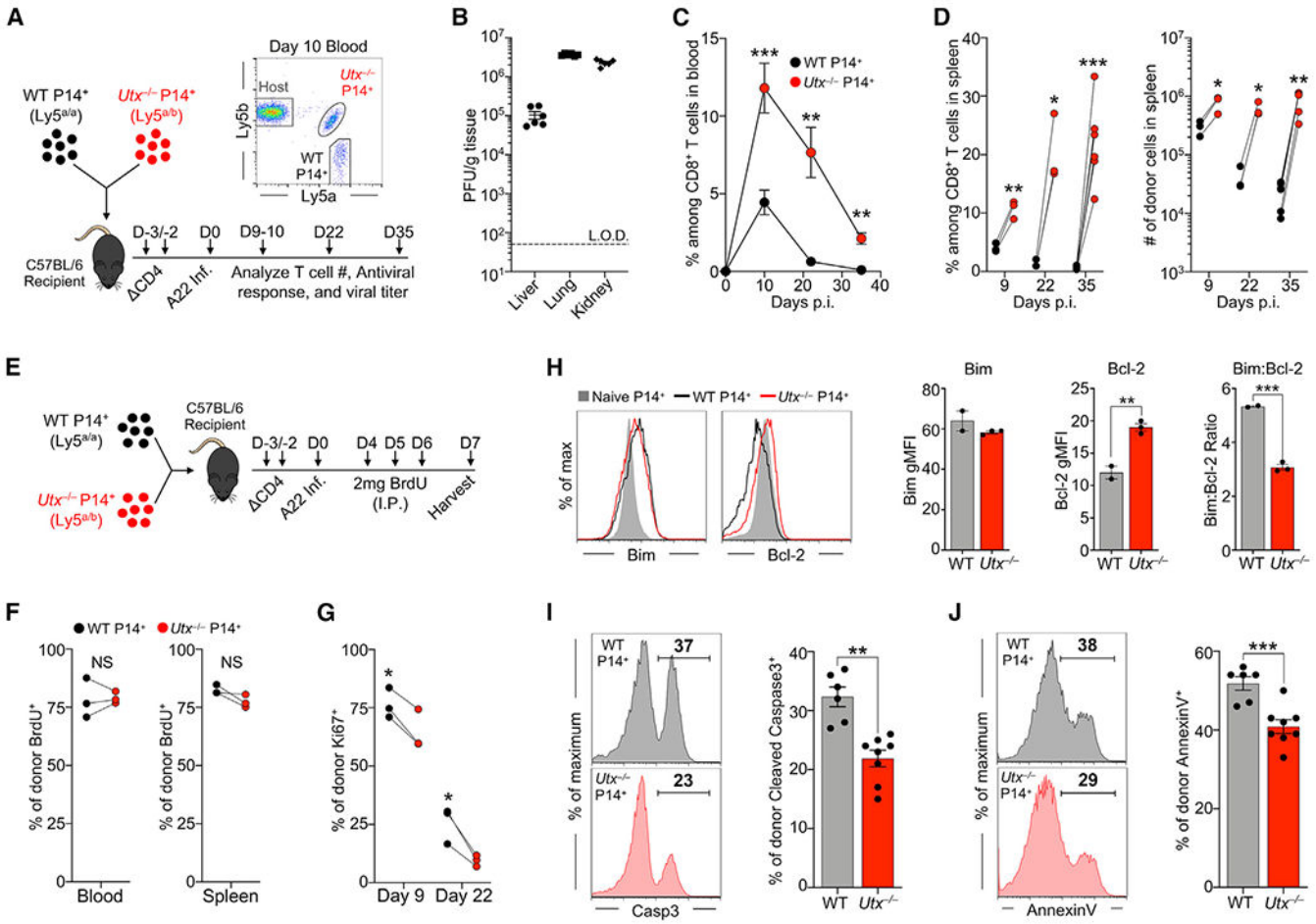

Figure 2. UTX limits CD8$^+$ T cell accumulation and maintenance

(A–G) WT and UTX-deficient P14$^+$CD8$^+$ T cells were introduced into the same recipients, followed by CD4 depletion and infection with LCMV-A22.

(A) The two donor CD8$^+$ T cell populations and host CD8$^+$ T cells were identified by surface expression of Ly5a and Ly5b.

(B) Infectious virus in livers, lungs, and kidneys at day 35 post-infection.

(C) The frequency of donor cells among all CD8$^+$ T cells in the blood at days 10, 22, and 35 post-infection. For illustrative purposes, donor populations are graphed separately yet were in the same mice.

(D) The frequency and number of donor cells in the spleen at days 9, 22, and 35 post-infection. Lines connect pairs of WT and UTX-deficient P14$^+$ cells present in each recipient.

(B)–(D) show one representative experiment of two independent experiments (n = 3–6).

(E and F) Recipient mice were treated with 2 mg of BrdU via intraperitoneal injection on days 4, 5, and 6 post-infection.

(E) Illustration of the approach.

(F) The percentage of donor cells staining positive for BrdU in the blood or spleen day 7 post-infection.

(G) The percentage of donor cells staining positive for Ki-67 in the spleen as determined by flow cytometry.

(F) and (G) show one representative experiment of two independent experiments (n = 3).
(H–J) WT and UTX-deficient $P14^{+}CD8^{+}$ T cells were introduced into separate mice, followed by CD4 depletion and infection with LCMV-A22. Cells were isolated at day 9 post-infection. Anti-BIM and anti-BCL2 fluorescence intensity were assessed directly *ex vivo*, and cleaved caspase-3 and annexin V staining were measured after brief culture.
(H) Representative plots display the expression of Bim and Bcl-2 in donor cells. Graphs show gMFI for BIM and BCL-2, as well as the ratio of BIM gMFI to BCL-2 gMFI. Data are from one of three independent experiments with 2–3 mice per group.
(I) Donor cells were cultured with $GP_{33–41}$ peptide for 5 h followed by quantification of intracellular cleaved caspase-3.
(J) Surface binding of annexin V following $GP_{33–41}$ stimulation.
Graphs in (I) and (J) show data compiled from three independent experiments with 6–8 mice per group.
Error bars display mean ± SEM. Significance was determined by a paired (C, D, F, and G) or unpaired (H and J) Student's test (*$p < 0.05$, **$p < 0.01$, ***$p < 0.001$).
See also Figures S3 and S4.

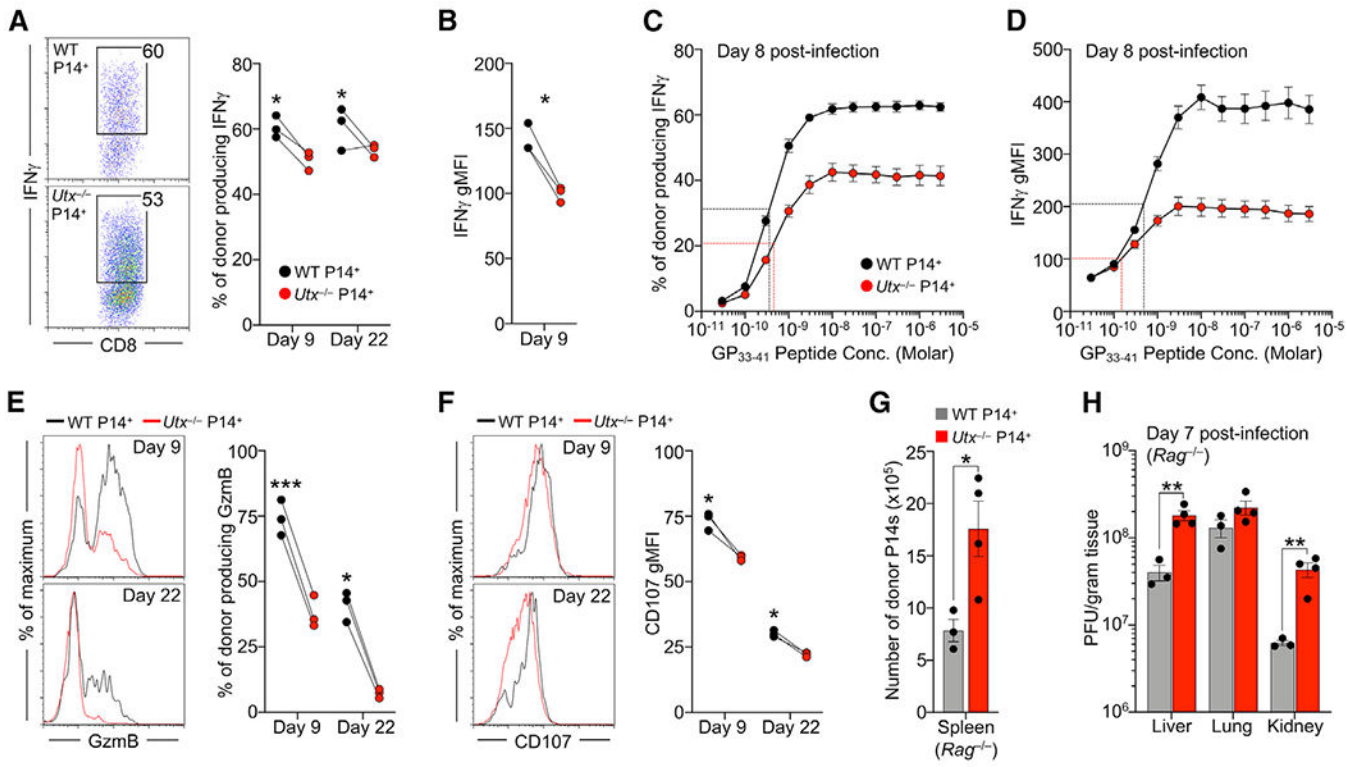

Figure 3. UTX supports the effector functions of virus-specific CD8$^+$ T cells

(A and B) WT and UTX-deficient P14$^+$ CD8$^+$ T cells were introduced into the same recipient mice, followed by CD4 depletion and infection with LCMV-A22. Splenocytes were harvested at days 9 or 22 and were stimulated with $GP_{33–41}$ peptide for 5 h followed by ICCS.

(A) The dot plot shows an example of IFNγ production by donor cells at day 9; the numbers represent the percentage of cells with the box. The graph shows cumulative data from three recipients and depicts the percentage of either donor that made IFNγ; the lines connect cells that were in the same host.

(B) The graph shows the gMFI of IFNγ among IFNγ^+ donor cells. Data from three recipients are shown.

(C and D) WT and *Utx*$^{-/-}$ P14$^+$CD8$^+$ T cells were introduced into separate recipients, followed by CD4 depletion and infection with LCMV-A22. Splenocytes were stimulated with different concentrations of $GP_{33–41}$ peptide followed by ICCS analysis. Data represent a single experiment (of two performed) with four mice per group.

(C) Percentage of donor P14s expressing IFNγ at each peptide concentration. The black and red lines indicate the half-maximal response.

(D) The gMFI of IFNγ among IFNγ^+ donor cells; the black and red lines indicate the half-maximal response.

(E) Using the dual transfer approach as described for (A) and (B), donor cells were analyzed for granzyme B expression; the lines connect donor cells that were present in the same infected hosts.

(F) Donor cell degranulation. Graph shows gMFI of CD107a/b gated on the indicated donor cells.

(A), (B), (E), and (F) show one of two independent experiments (n = 3 recipients).
(G and H) WT and UTX-deficient $P14^{+}CD8^{+}$ T cells were introduced into separate $Rag^{-/-}$ mice, followed by infection with LCMV-A22. Analyses were performed on day 7 post-infection.
(G) The number of donor cells per $Rag^{-/-}$ spleen.
(H) The viral titer in livers, lungs, and kidneys of the $Rag^{-/-}$ recipients.
(G) and (H) show one of two independent experiments with 3–4 $Rag^{-/-}$ recipients per group. Error bars display mean ± SEM. Significance was determined by a paired (A–F) or unpaired (G and H) Student's t test (*$p < 0.05$, **$p < 0.01$, ***$p < 0.001$).
See also Figure S5.

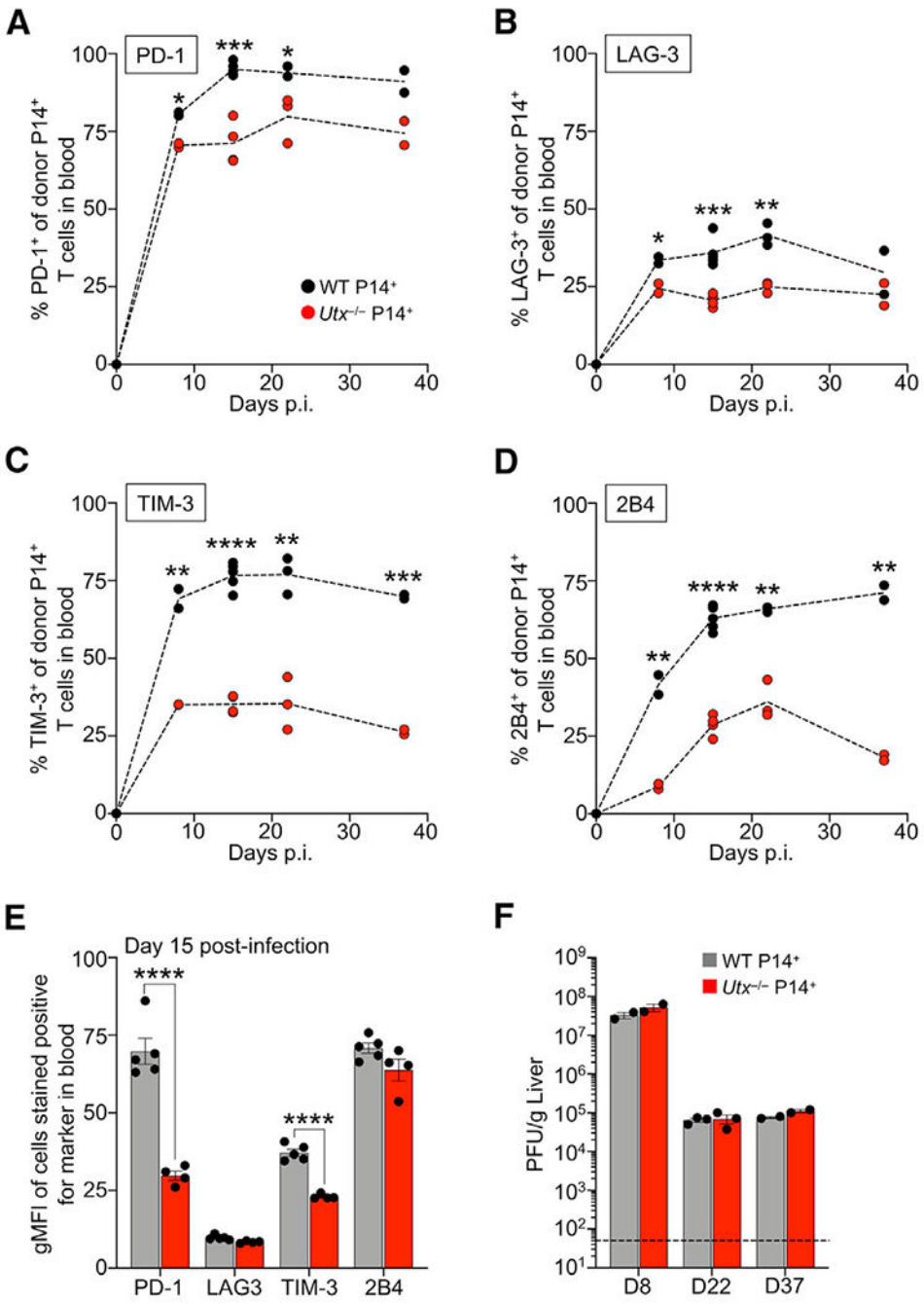

Figure 4. UTX increases inhibitory receptor expression

WT and UTX-deficient $P14^{+}CD8^{+}$ T cells were transferred into separate mice and analyzed for their expression of inhibitory receptors at multiple times after LCMV-A22 infection.

(A–D) Time course showing the percent of donor P14s expressing PD-1 (A), LAG-3 (B), TIM-3 (C), and 2B4 (D) in blood.

(E) The gMFI of inhibitory receptors on donor P14s collected from blood at day 15 post-infection. The measurement was determined for donor cells that stained positive for the indicated molecule.

(F) The viral titer in the liver at various days post-infection.

Data show one representative experiment of three independent experiments with 2–5 mice per group. Error bars display mean ± SEM. Significance was determined using an unpaired Student's t test (*p < 0.05, **p < 0.01, ***p < 0.001, ****p < 0.0001).

See also Figure S4.

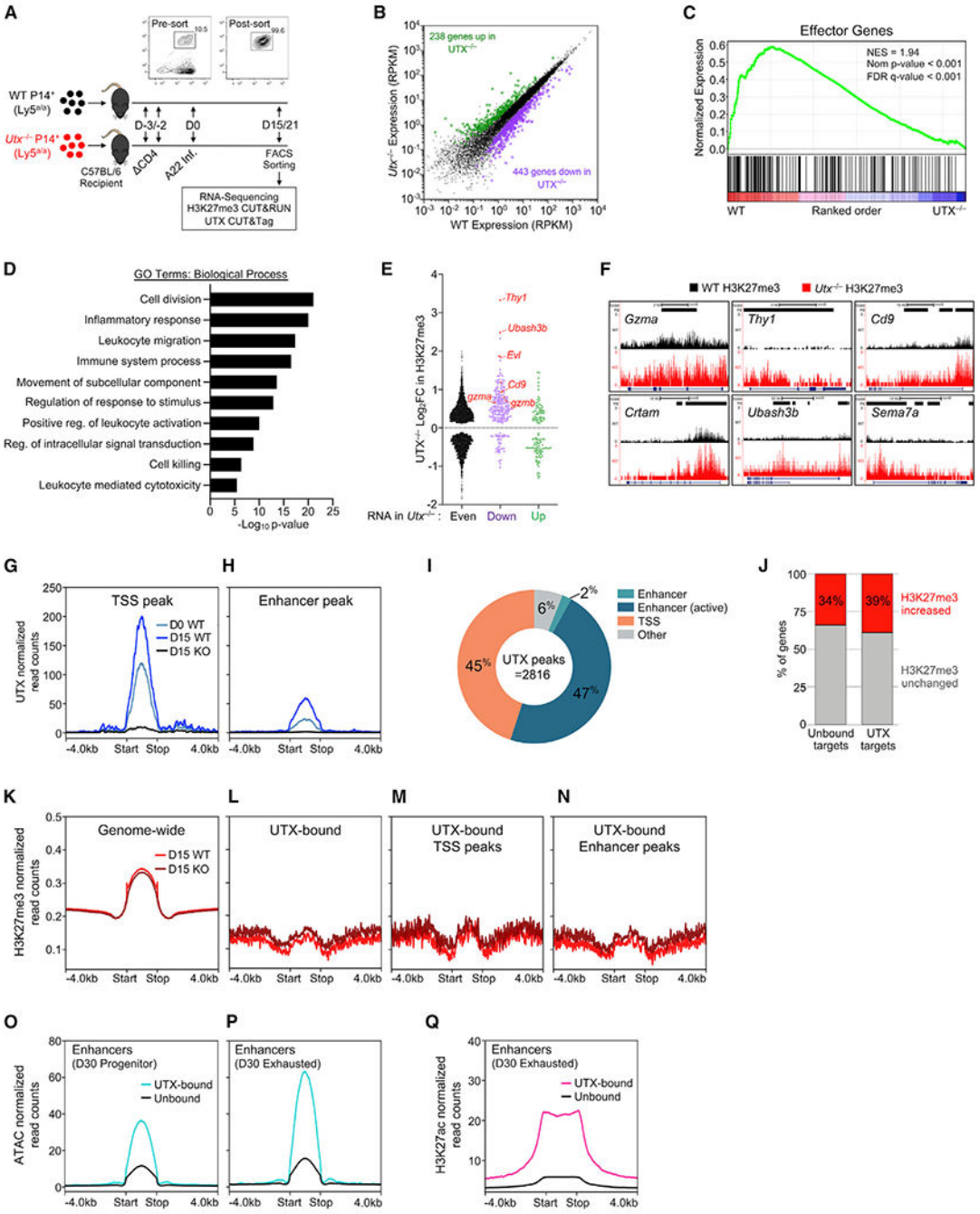

Figure 5. UTX alters gene expression in virus-specific CD8$^+$ T cells

(A) An illustration of the approach. WT and UTX-deficient P14$^+$CD8$^+$ T cells were introduced into the separate hosts, followed by CD4 depletion and infection with LCMV-A22. Donor cells from 3–4 mice were isolated by FACS at day 15 for H3K27me3 CUT&RUN or UTX CUT&Tag analyses or isolated at day 22 for RNA-seq analyses. (B) EdgeR analysis of RNA-seq data showing genes with significantly changed expression (FDR < 0.05; $\log_2$ fold change > |1.0|), comparing genes significantly downregulated in *Utx*

$^{-/-}$ donor P14^{+} T cells (purple) to those upregulated (green). RNA-seq data are derived from FACS donor cells from 3–4 recipient mice per group.

(C) GSEA of effector genes, ranked according to their relative expression in WT and *Utx*$^{-/-}$ cells. The genes in this gene set are known to be expressed in CTLs, but not naive cells.

(D) Genes showing significant differences in expression were subjected to GOrilla analysis followed by REVIGO analysis. The analysis identified several biological processes that are predicted to be significantly altered between WT and *Utx*$^{-/-}$ T cells based on differential gene expression.

(E) Isolated cells were subjected to H3K27me3 CUT&RUN analysis. The anti-H3K27me3-bound DNA fragments were eluted, sequenced, and quantified across the genome. The graph depicts the relative change in *Utx*$^{-/-}$ H3K27me3 density ($\log_2$ fold change) compared to WT for individual genes that were grouped based on changes in *Utx*$^{-/-}$ gene expression (RNA-seq in B). H3K27me3 changes are shown for genes having equal (black), significantly downregulated (purple), or significantly upregulated (green) RNA expression in *Utx*$^{-/-}$ P14s. The H3K27me3 CUT&RUN data are from four recipients per group.

(F) UCSC genome browser images of normalized H3K27me3 tracks at the *Gzma, Thy1, Cd9, Crtam, Ubash3b*, and *Sema7a* loci, showing mean values from four independent replicates of WT (black) or *Utx*$^{-/-}$ (red). The heavy bars depict regions with significantly enriched peaks of H3K27me3 in UTX-deficient P14 cells, compared to WT cells.

(G–I) UTX CUT&Tag was performed on WT CD8^{+} T cells at day 0 (n = 2) and day 15 post-infection (n = 4) and at day 15 for *Utx*$^{-/-}$ (KO) cells (n = 2).

(G and H) The average profile of UTX coverage is plotted based on normalized read counts for all UTX peaks of enrichment that occur at transcription start sites (TSSs; G) or enhancers (H). Enhancers were annotated based on published ATAC-seq datasets (Beltra et al., 2020). Start and stop define the boundary of the UTX peaks. Line colors indicate the profile for WT uninfected P14 (D0; light blue), WT at day 15 of LCMV infection (dark blue), or *Utx*$^{-/-}$ at day 15 (black).

(I) The pie graph depicts the proportion of UTX binding at TSSs, enhancers, active enhancers, and other locations (neither TSS nor enhancer) that are within 20 kb of TSSs. Active enhancer annotation was based on published H3K27ac datasets (Yao et al., 2019).

(J) H3K27me3 CUT&RUN changes were correlated with UTX binding at day 15 post-infection at genes showing reduced expression in *Utx*$^{-/-}$ T cells. *Utx*$^{-/-}$ misregulated genes were categorized as UTX bound or unbound, then contrasted for the percentage of these genes that experienced increased H3K27me3 in *Utx*$^{-/-}$ P14 cells.

(K and L) All H3K27me3 peaks of enrichment that failed to overlap with UTX peaks (UTX-unbound; K) are illustrated for comparison to UTX peaks near genes with reduced expression in *Utx*−/− cells (UTX-bound; L). The average profile of H3K27me3 coverage is plotted based on normalized read counts for WT (red) or *Utx*$^{-/-}$ P14 (dark red) samples.

(M and N) The UTX-bound H3K27me3 profiles in (L) were further subdivided into UTX peaks that overlap TSSs (M) or putative enhancers (N).

(O and P) Profiles of ATAC-seq normalized reads (Beltra et al., 2020) identify the open chromatin status of enhancers in “progenitor exhausted„ (Tex^{prog1}; O) or intermediate exhausted (Tex^{int}; P) T cells. These putative enhancers were subdivided based on overlap with UTX peaks of enrichment (UTX-bound; light blue profile) or peaks lacking UTX association (unbound; black profile).

(Q) The profile of H3K27ac ChIP-seq normalized reads (Yao et al., 2019) demonstrates enhancer activation status at regions that overlap with UTX binding (pink) compared to enhancers not bound by UTX (black).

See also Figure S6 and Tables S1, S2, S3, and S4.

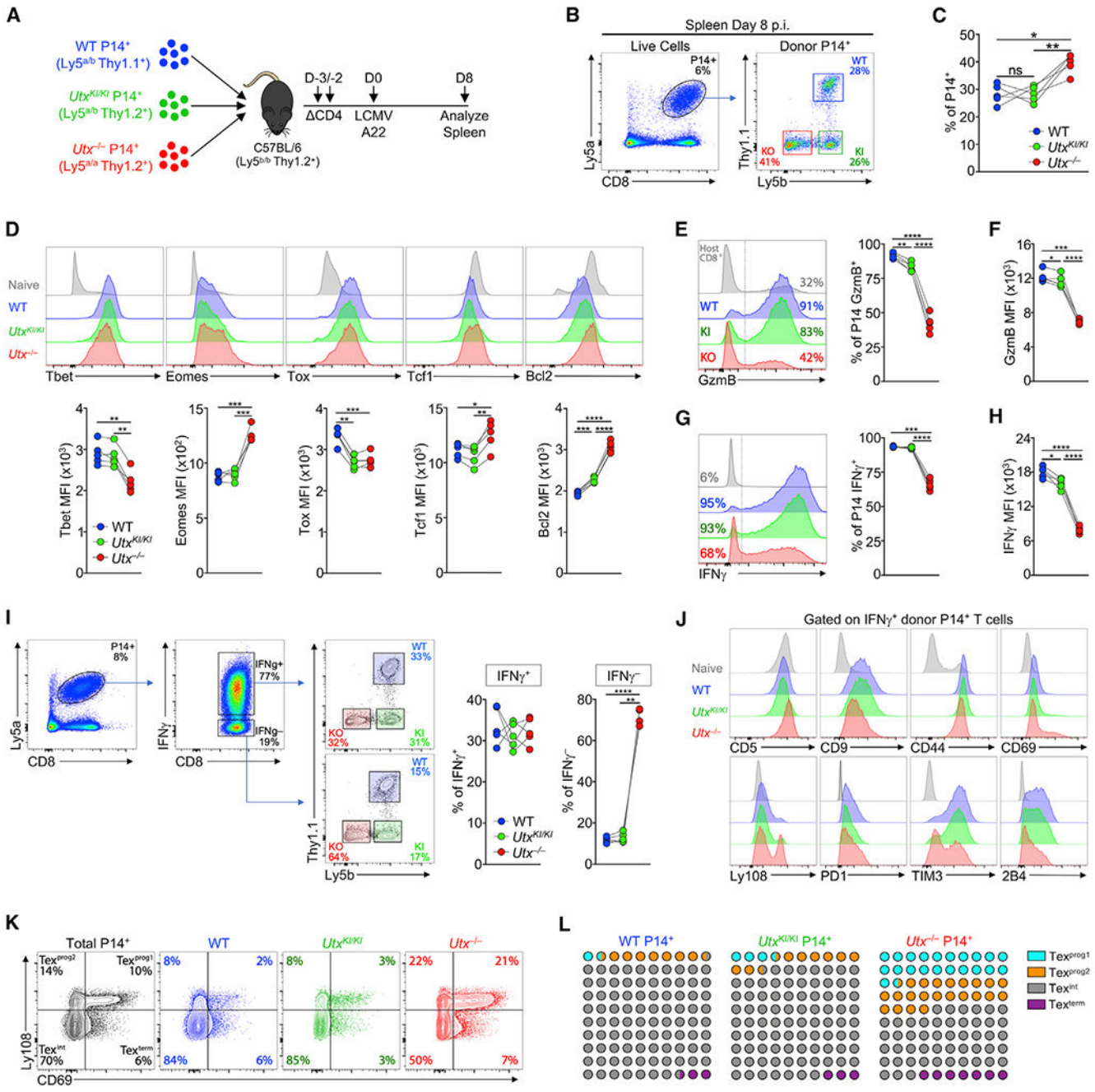

Figure 6. UTX demethylase activity is not required for effector CD8$^+$ T cell function during chronic infection

WT, UTX-KI (catalytic dead knockin), and UTX-KO P14$^+$CD8$^+$ T cells were introduced into the same recipients, followed by CD4 depletion and infection with LCMV-A22. At day 8 post-infection, splenic donor P14T cells were analyzed for surface marker expression, transcription factor levels, and cytokine expression.

(A) Illustration of the approach.

(B) The three donor P14 T cell populations and host CD8$^+$ T cells were identified by surface expression Ly5a, Ly5b, and Thy1.1.

(C) Frequency of each donor P14 group among all donor $CD8^+Ly5a^+$ P14 T cells in spleen. Lines connect pairs of WT, UTX-KI, and UTX-KO P14T cells present in each recipient.
(D) Histogram plots and gMFI for the transcription factors T-bet, Eomes, Tox, Tcf1, and Bcl2.
(E and F) The fraction of donor P14 T cells producing granzyme (E) and the gMFI of granzyme expression among granzyme-positive cells (F).
(G and H) The fraction of donor cells making IFNγ (G) and the gMFI among IFNγ-positive cells (H).
(I) The distribution of IFNγ^+ (left) and IFNγ^- (right) donor cell populations after re-stimulation with $GP_{33–41}$ peptide in an ICCS assay. The left graph shows the distribution of donor cells among the IFNγ^+ cells; the right graphs shows the distribution of donor cells that failed to make IFNγ.
(J) The histograms show several activation and inhibitory receptors expressed by IFNγ^+ donor cells.
(K) The surface expression of Ly108 and CD69 on each donor cell population was used to identify Tex^{prog1}, Tex^{prog2}, Tex^{int}, and Tex^{term} subsets.
(L) Distribution of the four developmental stages of exhaustion for donor cell populations. Each circle represents 1% of the total population.
Data show one experiment with five recipient mice. Samples from the five recipient mice were concatenated to generate histograms. Significance was determined by a paired Student's t test (*$p < 0.05$, **$p < 0.01$, ***$p < 0.001$, ****$p < 0.0001$).
See also Figure S7.

KEY RESOURCES TABLE

REAGENT or RESOURCE	SOURCE	IDENTIFIER
Antibodies		
Anti-BrdU, FITC, clone B44	BD Biosciences	Cat#347583; RRID: AB_400327
Anti-mouse Bcl-2, PE, clone 3F11	BD Biosciences	Cat#51-15025X; RRID: AB_396457
Anti-mouse Bim, PE, clone C34C5	Cell Signaling	Cat#2933S; RRID: AB_1030947
Anti-mouse CD3ε, BV421, clone 145-2C11	Biolegend	Cat#100335; RRID: AB_10898314
Anti-mouse CD3ε, PerCP, clone 145-2C11	Biolegend	Cat#100325; RRID: AB_893319
Anti-mouse CD3ε, purified, Ultra-LEAF, clone 145-2C11	Biolegend	Cat#100340; RRID: AB_11149115
Anti-mouse CD4, purified, InVivoMab, clone GK1.5	BioXcell	Cat#BE0003-1; RRID: AB_1107636
Anti-mouse CD4, FITC, clone GK1.5	Biolegend	Cat#100406; RRID: AB_312691
Anti-mouse CD4, PE, clone GK1.5	Biolegend	Cat#100408; RRID: AB_312693
Anti-mouse CD5, APC, clone 53-7.3	Invitrogen	Cat#17-0051-82; RRID: AB_469331
Anti-mouse CD8a, APC, clone 53-6.7	Biolegend	Cat#100712; RRID: AB_312751
Anti-mouse CD8a, biotinylated, clone 53-6.7	Biolegend	Cat#100704; RRID: AB_312743
Anti-mouse CD8a, BUV395, clone 53-6.7	BD Biosciences	Cat#563786; RRID: AB_2732919
Anti-mouse CD8a, BV421, clone 53-6.7	Biolegend	Cat#100737; RRID: AB_10897101
Anti-mouse CD8a, BV785, clone 53-6.7	Biolegend	Cat#100750; RRID: AB_2562610
Anti-mouse CD8a, FITC, clone 53-6.7	Biolegend	Cat#100706; RRID: AB_312745
Anti-mouse CD8a, PE, clone 53-6.7	Biolegend	Cat#100707; RRID: AB_312746
Anti-mouse CD8a, PerCP, clone 53-6.7	Biolegend	Cat#100732; RRID: AB_893427
Anti-mouse CD9, PE, clone MZ3	Biolegend	Cat#124806; RRID: AB_1279325
Anti-mouse CD16/32 (TruStain fcX), purified, clone 93	Biolegend	Cat#101320; RRID: AB_1574975
Anti-mouse CD28, purified, Ultra-LEAF, clone 37.51	Biolegend	Cat#102116; RRID: AB_11147170
Anti-mouse CD44, AF700, clone IM7	Invitrogen	Cat#56-0441-82; RRID: AB_494011
Anti-mouse CD44, FITC, clone IM7	Biolegend	Cat#103006; RRID: AB_312957
Anti-mouse CD45.1 (Ly5a), APC, clone A20	Biolegend	Cat#110714; RRID: AB_313503
Anti-mouse CD45.1 (Ly5a), FITC, clone A20	Biolegend	Cat#110706; RRID: AB_313495
Anti-mouse CD45.1 (Ly5a), PE, clone A20	Biolegend	Cat#110707; RRID: AB_313497
Anti-mouse CD45.1 (Ly5a), PE/Cy7, clone A20	Biolegend	Cat#110730; RRID: AB_1134168
Anti-mouse CD45.2 (Ly5b), APC, clone 104	Biolegend	Cat#109814; RRID: AB_389211
Anti-mouse CD45.2 (Ly5b), BV605, clone 104	Biolegend	Cat#109841; RRID: AB_2563485
Anti-mouse CD45.2 (Ly5b), FITC, clone 104	Biolegend	Cat#109806; RRID: AB_313443
Anti-mouse CD45.2 (Ly5b), PE, clone 104	Biolegend	Cat#109807; RRID: AB_313444
Anti-mouse CD45.2 (Ly5b), PerCP/Cy5.5, clone 104	Biolegend	Cat#109828; RRID: AB_893350
Anti-mouse CD62L, APC, clone MEL-14	Biolegend	Cat#104411; RRID: AB_313098
Anti-mouse CD69, APC, clone H1.2F3	Biolegend	Cat#104514; RRID: AB_492843
Anti-mouse CD69, FITC, clone H1.2F3	Biolegend	Cat#104506; RRID: AB_313109
Anti-mouse CD69, PE, clone H1.2F3	Biolegend	Cat#104508; RRID: AB_313111

REAGENT or RESOURCE	SOURCE	IDENTIFIER
Anti-mouse CD90.1 (Thy1.1), AF700, clone OX-7	Biolegend	Cat#202527; RRID: AB_1626244
Anti-mouse CD90.1 (Thy1.1), PE, clone OX-7	Biolegend	Cat#202523; RRID: AB_1595635
Anti-mouse CD90.2 (Thy1.2), APC, clone 53-2.1	eBioscience	Cat#17-0902-82; RRID: AB_469422
Anti-mouse CD90.2 (Thy1.2), PE, clone 30-H12	Biolegend	Cat#105308; RRID: AB_313179
Anti-mouse CD107a (LAMP-1), FITC, clone 1D4B	Biolegend	Cat#121605; RRID: AB_572006
Anti-mouse CD107b (LAMP-2), FITC, clone eBioABL-93	eBioscience	Cat#11-1072-81; RRID: AB_657579
Anti-mouse CD127 (IL-7Ra), APC, clone A7R34	Biolegend	Cat#135011; RRID: AB_1937217
Anti-mouse CD223 (LAG3), APC, clone C9B7W	Biolegend	Cat#125209; RRID: AB_10639935
Anti-mouse CD223 (LAG3), PE, clone C9B7W	Biolegend	Cat#125207; RRID: AB_2133344
Anti-mouse CD244.2 (2B4), PE, clone m2B4 (B6) 458.1	Biolegend	Cat#133507; RRID: AB_1626231
Anti-mouse CD279 (PD-1), BV421, clone RMP1-30	Biolegend	Cat#109121; RRID: AB_2687080
Anti-mouse CD279 (PD-1), PE, clone RMP1-30	Biolegend	Cat#109104; RRID: AB_313421
Anti-mouse CD366 (TIM-3), BV605, clone RMT3-23	Biolegend	Cat#119721; RRID: AB_2616907
Anti-mouse CD366 (TIM-3), PE, clone RMT3-23	Biolegend	Cat#119703; RRID: AB_345377
Anti-mouse EOMES, PE, clone Dan11mag	eBioscience	Cat#12-4875-82; RRID: AB_1603275
Anti-mouse Granzyme B, AF647, clone GB11	Biolegend	Cat#515405; RRID: AB_2294995
Anti-mouse Granzyme-B, FITC, clone GB11	Biolegend	Cat#515403; RRID: AB_2114575
Anti-mouse IFN-γ, APC, clone XMG1.2	Biolegend	Cat#505810; RRID: AB_315404
Anti-mouse IFN-γ, BV421, clone XMG1.2	BD Biosciences	Cat#563376; RRID: AB_2738165
Anti-mouse IFN-γ, FITC, clone XMG1.2	Biolegend	Cat#505806; RRID: AB_315400
Anti-mouse IFN-γ, PE/Cy7, clone XMG1.2	eBioscience	Cat#25-7311-82; RRID: AB_469680
Anti-mouse IL-2, APC, clone JES6-5H4	Biolegend	Cat#503810; RRID: AB_315304
Anti-mouse Ki67, FITC, clone B56	BD Biosciences	Cat#556026; RRID: AB_396302
Anti-mouse KLRG1, PE, clone 2F1/KLRG1	Biolegend	Cat#138407; RRID: AB_10574005
Anti-mouse Ly108, APC, clone 330-AJ	Biolegend	Cat#134610; RRID: AB_2728155
Anti-mouse Ly108, PE, clone 330-AJ	Biolegend	Cat#134606; RRID: AB_2188095
Anti-mouse TNF, APC, clone MP6-XT22	Biolegend	Cat#506308; RRID: AB_315429
Anti-mouse TOX, APC, clone REA473	Miltenyi Biotec	Cat#130-118-335; RRID: AB_2751485
Anti-mouse Vα2, PE, clone B20.1	Biolegend	Cat#127808; RRID: AB_1134183
Anti-mouse Vβ8.1/8.2, FITC, clone KJ16-133.18	Biolegend	Cat#118406; RRID: AB_1227786
Anti-rabbit IgG (H+L), F(ab')$_2$ fragment, AF647	Cell Signaling	Cat#4414S; RRID: AB_10693544
Anti-T-bet, PE, clone 4B10	Biolegend	Cat#644810; RRID: AB_2200542
Goat anti-rat IgG, AF488, clone Poly4054	Biolegend	Cat#405418; RRID: AB_2563120
Guinea Pig anti-rabbit IgG, purified	Fisher	Cat# NBP172763
Hamster IgG isotype control, PE, clone A19-3	BD Biosciences	Cat#51-66995X; RRID: AB_395172
Histone H3 XP rabbit mAb, purified, clone D1H2	Cell Signaling	Cat#4499S; RRID: AB_10544537
Rabbit anti-cleaved Caspase-3, biotinylated, clone C292-605	BD Biosciences	Cat#550557; RRID: AB_393750
Rabbit anti-H3K27me3 mAb, purified, clone C36B11	Cell Signaling	Cat#9733s; RRID: AB_2616029
Rabbit anti-Histone H3 XP mAb, purified, clone D1H2	Cell Signaling	Cat#4499S; RRID: AB_10544537

REAGENT or RESOURCE	SOURCE	IDENTIFIER
Rabbit anti-TCF1 mAb, AF647, clone C63D9	Cell Signaling	Cat#6709S; RRID: AB_2797631
Rabbit anti-UTX mAb, purified, clone D3Q1I	Cell Signaling	Cat#33510s; RRID: AB_2721244
Rabbit mAb IgG XP isotype control, purified, clone DA1E	Cell Signaling	Cat#4096s; RRID: AB_1642334
Bacterial and virus strains		
LCMV-Armstrong	Whitmire lab	N/A, generated in house
LCMV-A22	Whitmire lab	N/A, generated in house
LCMV-Clone13	Whitmire lab	N/A, generated in house
Chemicals, peptides, and recombinant proteins		
ACK Lysing Buffer	Lonza	Cat#10-548E
Annexin V-FITC	Biolegend	Cat#640906
Biotinylated $DbGP_{33-41}$ Monomer	NIH Tetramer core	N/A
Biotinylated $DbNP_{396-404}$ Monomer	NIH Tetramer core	N/A
Bovine Serum Albumin	Sigma-Aldrich	Cat#A4503
Brefeldin A Solution (1000X)	Biolegend	Cat#420601
Bromodeoxyuridine	Sigma-Aldrich	Cat#B5002
Concanavalin-A beads	Polysciences	Cat# 86057-3
Digitonin	Millipore	Cat# 300410-1GM
DNase-I	Sigma-Aldrich	Cat#D4527
DMEM	Lonza	Cat#12-61F
EMEM	Sigma-Aldrich	Cat#56416C
FBS	GIBCO	Cat#26140-079
Ficoll	GE Healthcare	Cat#17-1440-02
Fixation Buffer	Biolegend	Cat#420801
FoxP3 Fix/Perm Buffer Set	Biolegend	Cat#421403
Ghost Red780 Viability Dye	Tonbo Biosciences	Cat#13-0865
Ghost UV450 Viability Dye	Tonbo Biosciences	Cat#13-0868
HEPES	Lonza	Cat#17-737E
Histopaque-1077		N/A
Intracellular Permeabilization Buffer	Biolegend	Cat#421002
L-glutamine	Lonza	Cat#17-605L
MojoSort Buffer	Biolegend	Cat#480017
Monensin (1000X)	Biolegend	Cat#420701
NEBNext HiFi 2x PCR Master Mix	NEB	Cat# M0541L
OmniPur Ethidium Bromide	Calbiochem	Cat#18H235208
Penicillin-Streptomycin	Lonza BioWhittaker	Cat#BW17602E
RPMI 1640	Lonza	Cat#12-167F
Sodium Pyruvate	Lonza	Cat#13-115E
Streptavidin-Allophycocyanin	Life Technologies	Cat#S868
Streptavidin-PE	Biolegend	Cat#405203

REAGENT or RESOURCE	SOURCE	IDENTIFIER
Taq DNA polymerase	Invitrogen	Cat#18038042
TBE Buffer, Molecular Biology Grade	Calbiochem	Cat#574795
TRIZOL LS Reagent	Ambien	Cat#10296028
True-Nuclear Transcription Factor Buffer Set	Biolegend	Cat#424401
UltraPure Agarose	Invitrogen	Cat#16500
Zombie Aqua Fixable Viability Dye	Biolegend	Cat#423101
Zombie Green Fixable Viability Dye	Biolegend	Cat#423111
2-Methylcyclohexanol	Sigma-Aldrich	Cat#M7522
3-x-Flag-pA-Tn5-FL	Addgene	Cat# 124601
7-AAD Viability Staining Solution	Biolegend	Cat#420403
Critical commercial assays		
DNeasy Isolation Kit	QIAGEN	Cat#69504
KAPA dual index adapters	Roche	KK8722
KAPA HyperPrep Kit	Roche	KK8504
KAPA mRNA HyperPrep Kit	Roche	KK8580
KAPA Pure Beads	Roche	KK8000
KAPA Stranded mRNA-Seq Kit, with KAPA mRNA Capture Beads	Roche	Cat#07962193001
MojoSort Mouse CD8 T Cell Isolation Kit	Biolegend	Cat#480008
MojoSort Streptavidin Nanobeads	Biolegend	Cat#480016
UltraComp eBeads Compensation beads	ThermoFisher Scientific	Cat#01-2222-41
Deposited data		
RNA seq: $CD8^+$ T cells; spleen	This paper	GEO Accession GSE143736
CUT&RUN DNA seq: $CD8^+$ T cells; spleen	This paper	GEO Accession GSE143736
CUT&Tag DNA-seq: $CD8^+$ T cells; spleen	This paper	GEO Accession GSE143736
Experimental models: Cell lines		
Vero-E6	Michael Buchmeier	The Scripps Research Institute, La Jolla, CA
BHK-21	American Type Culture Collection	Cat#CCL-10
Experimental models: Organisms/strains		
Mouse: C57BL/6J	Jackson Laboratory (purchased during last 7 years, bred at UNC)	Cat#000664
Mouse: B6.Ly5a (CD45.1)	Jackson Laboratory (purchased during last 7 years, bred at UNC)	Cat#002014
Mouse: Lck-Cre	Jackson Laboratory (purchased during last 7 years, bred at UNC)	Cat#003802

REAGENT or RESOURCE	SOURCE	IDENTIFIER
Mouse: $UTX^{fl/fl}$	Backcrossed to B6/J in Whitmire lab	PMID:23028370
Mouse: $UTX^{KI/KI}$	Backcrossed to B6/J in Whitmire lab	PMID: 29073101
Mouse: $P14^{+}$ TCR-Tg (B6.Ly5a)	Backcrossed in Whitmire lab	PMID:2573841
Oligonucleotides		
Genotyping for Lck-Cre (FW)	TGCAACGAGTG ATGAGGTTC	N/A
Genotyping for Lck-Cre (RV)	ACAGCATTGCT GTCACTTGG	N/A
Genotyping for UTX (FW1)	TCCGAGAAAG GAAATGTGAG	N/A
Genotyping for UTX (FW2)	GTGGGCCAGTA CAAAACCAC	N/A
Genotyping for UTX (RV)	GATTGGTCTAA TTTGGCACC	N/A
Genotyping for UTX-KI/KI (FW1)	GCCAAGCAGCC TATCAAAGC	N/A
Genotyping for UTX-KI/KI (RV1)	GAAGTTGTTAT TTTCTTGATG	N/A
Genotyping for UTX-KI/KI (RV2)	GAAGTTGTTAT TTGCCTGAGC	N/A
Software and algorithms		
BEDTools		Quinlan and Hall, 2010 (PMID: 20110278)
Bowtie2	Johns Hopkins University	http://bowtie-bio.sourceforge.net/bowtie2/index.shtml
deepTOOLs		Ramírez et al., 2016 (PMID: 27079975)
HOMER		Heinz et al., 2010 (PMID: 20513432)
TopHat (2.1.1)	Johns Hopkins University	https://ccb.jhu.edu/software/tophat/index.shtml
MACS2		https://github.com/macs3-project/MACS
hiddenDomains	UNC-Chapel Hill	http://hiddendomains.sourceforge.net/
EdgeR	Walter and Eliza Hall Institute	http://www.bioconductor.org/packages/release/bioc/html/edgeR.html
FlowJo Software (version 9.9.6 and 10.7.1)	Tree Star	https://www.flowjo.com
Gene Ontology Browser	JAX	http://www.informatics.jax.org
Genome Analyzer Pipeline Software	Casava v1.9	https://www.illumina.com
GraphPad Prism (version 9.0.2)	GraphPad	https://www.graphpad.com